

Beyond spin-1/2: Multipolar spin-orbit coupling in noncentrosymmetric crystals with time-reversal symmetry

Masoud Bahari,^{1,2,*} Kristian Mæland,^{1,2} Carsten Timm,^{2,3} and Björn Trauzettel^{1,2}

¹*Institute for Theoretical Physics and Astrophysics, University of Würzburg, D-97074 Würzburg, Germany*

²*Würzburg-Dresden Cluster of Excellence ct.qmat, Germany*

³*Institute of Theoretical Physics, Technische Universität Dresden, 01062 Dresden, Germany*

(Dated: February 5, 2026)

We develop a symmetry-adapted multipolar $\mathbf{k} \cdot \mathbf{p}$ theory close to the bulk Γ point for time-reversal-symmetric, noncentrosymmetric C_{3v} crystals in the strong atomic spin-orbit-coupling (jj -coupling) limit. Using a $j \in \{1/2, 3/2, 5/2\}$ multiplet basis appropriate for heavy-element p - and d -bands, we systematically construct all symmetry-allowed spin-orbit coupling terms up to fifth order in momentum and generalize the usual spin texture to a total-angular-momentum texture. For $j > 1/2$, multipolar spin-orbit coupling qualitatively reshapes Fermi surfaces and makes the topology of Bloch states band dependent. This leads to anisotropic high- j textures that go beyond a single Rashba helix. We classify these textures by their total-angular-momentum vorticity W_n for every energy band and identify distinct $|W_n| = 1, 2, 5$ phases. We show that their crossovers generate enhanced and nonmonotonic current-induced spin-polarization responses, namely the Edelstein effect, upon tuning the chemical potential. Our results provide a symmetry-based framework for analyzing and predicting multipolar spin-orbit coupling, total-angular-momentum textures, and spintronic responses in heavy-element materials without an inversion center.

I. INTRODUCTION

Spin-orbit coupling (SOC) in crystals without inversion symmetry gives rise to spin-split bands and momentum-dependent spin textures that underpin a broad range of phenomena in contemporary condensed-matter physics [1–21]. This ranges from topological insulators and semimetals to spintronic interfaces and unconventional superconductors [2, 9–16]. In such systems, the expectation value of the spin as a function of crystal momentum defines a texture on the Fermi surface that directly controls magnetoelectric responses [17], spin torques [18, 19], and the conversion between charge and spin currents [20, 21].

On surfaces and in bulk materials with C_{3v} symmetry, SOC effects are particularly rich. Beyond the paradigmatic linear Rashba model, higher-order terms in momentum generate hexagonally warped Fermi surfaces and spin textures with sizeable out-of-plane components, as extensively discussed for topological-insulator surfaces and Rashba alloys such as Bi_2Te_3 and $\text{Bi}/\text{Ag}(111)$ [22–25]. Recent work has shown that these higher-harmonic SOC contributions and the associated winding patterns of the spin texture are generic in systems with strong SOC and broken inversion symmetry, appearing in both surfaces and bulk crystals, including ferroelectric oxides and van der Waals heterostructures with radial Rashba fields [26–30]. This motivates a systematic treatment of SOC beyond the Rashba form, especially in three-dimensional materials, where the full point-group symmetry and the k_z dependence of the dispersion play an essential role.

Most theoretical analyses of spin-orbit-coupled materials, however, still build on single-band or effective spin-1/2 models. In this case, the orbital character is weak and the internal (spin) degree of freedom is encoded in the spin texture $\langle \sigma \rangle$ of the Bloch bands [25, 26, 28, 29, 31–36]. This picture implicitly treats the spin as an isolated two-level system and works well as long as orbital degrees of freedom and higher total angular momentum (TAM) components can be ignored. However, in many materials involving heavy p -, d -, or f -electron elements where SOC is strong, this assumption breaks down. Then, spin is no longer a good quantum number. Nevertheless, the TAM is typically a good quantum number in these materials. Consequently, the low-energy bands can be associated with their TAM j , which can be larger than 1/2, e.g., $j = 3/2$ or $j = 5/2$ [37–40].

While many nonmagnetic semiconductors are well described by effective spin-1/2 bands, materials built from lighter elements can also realize $j = 3/2$ low-energy manifolds. This occurs, for instance, near fourfold band degeneracies in cubic crystals, whereas higher-multiplicity crossings are comparatively rare. Such higher-fold degeneracies can nevertheless be enforced by symmetry in certain nonsymmorphic space groups [41].

In the spin-1/2 case, the Pauli matrices satisfy $\hat{\sigma}_i^2 = 1$ and the product of two different Pauli matrices is the third one. In this case, the set of the identity matrix and the Pauli matrices is closed under multiplication and prohibits building non-trivial higher-multipolar operators. By contrast, in higher- j manifolds, the angular-momentum operators obey $\hat{J}_i^2 \neq 1$ and the products of angular-momentum matrices are higher multipoles. Therefore, the spin density matrix acquires a genuine multipolar structure containing quadrupolar, octupolar, and higher-rank components [42–50].

For $j > 1/2$ electrons, the natural analogue of the fa-

* masoud.bahari@uni-wuerzburg.de

miliar spin texture is the texture of the TAM, defined by the expectation value $\langle \hat{\mathbf{J}} \rangle$ in the Bloch eigenstates. It characterizes how the average TAM vector (or, more generally, the corresponding set of multipoles) varies as a function of crystal momentum. Clarifying the distinction between conventional spin-1/2 textures $\langle \hat{\sigma} \rangle$ and TAM textures $\langle \hat{\mathbf{J}} \rangle$ is therefore crucial for correctly capturing the momentum-space structure of internal degrees of freedom.

In this work, we develop a general multipolar SOC description in time-reversal-symmetric, non-centrosymmetric C_{3v} crystals, where we treat the TAM explicitly in the multiplets $j \in \{1/2, 3/2, 5/2\}$. Using point group symmetry together with time-reversal symmetry (the gray group $C_{3v}+T$) and a double-group representation analysis, we systematically construct all SOC terms allowed near the Γ point, up to fifth order in momentum, by combining momentum polynomials and TAM-tensor matrices that transform as the trivial irreducible representation (irrep). This procedure yields a modified Rashba channel that is present for all j , together with genuinely high-rank multipolar SOC terms that exist only for $j > 1/2$. The latter acts within and between different j sectors and introduce m_j -dependent energy shifts and multipolar analogues of Rashba coupling that cannot be captured by effective spin-1/2 models.

We demonstrate that these multipolar SOC terms naturally generate Fermi surfaces with nontrivial spin textures that go far beyond a single helical Rashba pattern. In particular, the interplay between linear, cubic, and quintic SOC invariants gives rise to vorticity phase diagrams in which the TAM texture exhibits conventional single winding, as well as double and fivefold windings around the Γ point, depending on the momentum and the relative strength of the SOC channels.

Furthermore, we show that the higher-rank multipolar couplings can split heavy- and light-mass bands, induce strong interband hybridization, and give rise to highly anisotropic TAM textures with unconventional winding numbers (e.g., $W \in \{2, 5\}$). In the corresponding TAM-vorticity phase diagram, the heavy-mass bands dominated by $|j, m_j\rangle$ states with $|m_j| > 1/2$ are markedly more anisotropic than the light-mass $|j, \pm 1/2\rangle$ bands. This enhanced anisotropy arises from the emergence of multipolar SOC terms, which generate higher-order \mathbf{k} dependence of the effective spin-orbit field.

Moreover, within a semiclassical Boltzmann framework, we then compute the Edelstein susceptibility for the multiband textures generated by our $\mathbf{k} \cdot \mathbf{p}$ model [51–54]. We demonstrate that high- j multiplets and multipolar SOC lead to a strongly enhanced and non-monotonic charge-to-TAM response as a function of chemical potential. This contrasts with the smooth behavior of the conventional Rashba model. In particular, we find plateau-like structures and moderate changes in the Edelstein tensor whenever the Fermi level crosses between different j multiplets.

Particularly appealing platforms in this context are

non-centrosymmetric compounds such as PtBi_2 and BiTeI , both realizing bulk C_{3v} point group symmetry [55–63]. The former (latter) exhibits Weyl semimetal and unconventional superconductivity phases [63–68] (giant bulk Rashba-type SOC [55]). For PtBi_2 , density-functional theory reveals strongly spin-orbit-coupled p - and d -orbital-derived multiplets in the vicinity of the Fermi energy, which are naturally organized into $j = 3/2$ and $j = 5/2$ manifolds [61]. In BiTeI , by contrast, the low-energy bands are dominated by Bi and Te/I p states that form the canonical $j = 1/2$ and $j = 3/2$ multiplets of a giant Rashba semiconductor. Taken together, these materials are candidates for realizing multipolar and complex three-dimensional TAM textures.

Our analysis identifies the distinct roles of m_j -dependent energy shifts and multipolar Rashba terms in shaping the Edelstein response and suggests that C_{3v} materials with strong SOC, such as PtBi_2 , are promising platforms for engineering large and tunable Edelstein effects, complementing existing proposals based on interfaces, Weyl semimetals, and two-dimensional materials [27, 29, 69–73].

The remainder of this paper is organized as follows. In Sec. II, we develop the symmetry-constrained $\mathbf{k} \cdot \mathbf{p}$ Hamiltonian for time-reversal-symmetric, non-centrosymmetric C_{3v} systems, working in the $j \in \{1/2, 3/2, 5/2\}$ basis. Symmetry properties of our model are discussed in Sec. III. In addition, in Sec. IV, we propose a comprehensive analysis of the spin-split spectrum in $j > 1/2$ basis. In Sec. V, we analyze the resulting Fermi-surface TAM textures and vorticity phase diagrams, highlighting the emergence of higher-winding TAM textures and their manifestations in warped constant-energy contours. In Sec. VI, we compute the Edelstein tensor within a semiclassical Boltzmann approach and show how multipolar SOC enhances and reshapes the current-induced TAM polarization as the chemical potential is tuned. Finally, in Sec. VII, we summarize our main results and discuss experimental implications for related C_{3v} materials. The decomposition of j into the appropriate irreps is given in Appendix A. Further details on the transformation of the high- j basis and momentum under the point group are provided in Appendix B. The complete SOC model is presented in Appendix C. A summary of effective model Hamiltonians for $j = 1/2$ and $j \in \{3/2, 5/2\}$ are given in Appendix D. In Appendix E, we explain how one can compute TAM texture from first-principle calculations.

II. MODEL HAMILTONIAN

We analytically derive a $\mathbf{k} \cdot \mathbf{p}$ model Hamiltonian to quantify the strong SOC near the Γ point in the three-dimensional (3D) bulk Brillouin zone of a system with C_{3v} point group symmetry and time-reversal symmetry. The system features three mirror planes $\{\sigma_{v_1}, \sigma_{v_2}, \sigma_{v_3}\}$ intersecting at a threefold rotational axis $\{C_{3z}, C_{3z}^2\}$,

forming a trigonal pyramidal structure with C_{3v} point group symmetry [74, 75]. In the strong atomic spin-orbit regime, we employ jj coupling, where l and s are entangled into $j = l + s$ and the l manifold splits into $j \in \{l - 1/2, l + 1/2\}$. We then project onto the $j = 3/2$ (p -derived) and $j = 5/2$ (d -derived) subspaces relevant near the Fermi level.

The C_{3v} crystal field reduces the j multiplets according to $j = 5/2 \rightarrow 2\Gamma_4 \oplus \Gamma_5 \oplus \Gamma_6$ and $j = 3/2 \rightarrow \Gamma_4 \oplus \Gamma_5 \oplus \Gamma_6$, where Γ_4 is the two-dimensional spinor irrep and Γ_5, Γ_6 are one-dimensional complex-conjugate spinor irreps of the C_{3v} double group [74, 76, 77], see Appendix A. Even though each irrep is one dimensional in $\Gamma_5 \oplus \Gamma_6$, they pair into a Kramers doublet at the Γ point as enforced by time-reversal symmetry. These properties can be observed, for instance, for $j = 3/2$ electrons, in Fig. 1(a) where band splitting happens in $\Gamma - L(H)$ directions.

To incorporate Kramers' degeneracy into our model, we include time-reversal symmetry T in the C_{3v} point group. The resulting full group is given by $\mathcal{M}_{3v} = C_{3v} + TC_{3v}$, where \mathcal{M}_{3v} denotes the gray magnetic point group formed by combining C_{3v} with time-reversal symmetry. In this case, the character table doubles in terms of both the number of group elements and the number of irreps [49]. Each group element $g \in C_{3v}$ acquires a time-reversed partner $Tg \in TC_{3v}$. In the nonmagnetic C_{3v} group, the irreps are given by $\Gamma \in \{A_1, A_2, E\}$. We employ an orthogonal corepresentation scheme by separating time-reversal-even and -odd operators at the group-theory level. In this case, the total number of irreps is doubled in the magnetic group \mathcal{M}_{3v} : $\Gamma \in \{\Gamma_-, \Gamma_+\}$, where $\Gamma_{\pm} \in \{A_{1,\pm}, A_{2,\pm}, E_{\pm}\}$ and the \pm sign indicates whether the irrep is even or odd under time-reversal.

We begin by obtaining the matrix representation of the TAM vector $\hat{\mathbf{J}} = (\hat{J}_x, \hat{J}_y, \hat{J}_z)$ obeying SU(2) algebra in four- and six-dimensional representations for $j = 3/2$ and $j = 5/2$ basis, respectively. The multiband normal state model Hamiltonian takes the form $H = \sum_{\mathbf{k}} \hat{\psi}_{\mathbf{k}}^{\dagger} \hat{H}(\mathbf{k}) \hat{\psi}_{\mathbf{k}}$ where $\hat{\psi}_{\mathbf{k}}$ with

$$j = \frac{3}{2} : \hat{\psi}_{\mathbf{k}} = (c_{3/2}, c_{1/2}, c_{-1/2}, c_{-3/2})^T, \quad (1)$$

$$j = \frac{5}{2} : \hat{\psi}_{\mathbf{k}} = (c_{5/2}, c_{3/2}, c_{1/2}, c_{-1/2}, c_{-3/2}, c_{-5/2})^T, \quad (2)$$

where $c_{m_j, \mathbf{k}}^{\dagger}$ ($c_{m_j, \mathbf{k}}$) denotes the fermionic creation (annihilation) operator labeled with the 3D momentum $\mathbf{k} \in (k_x, k_y, k_z)$ and magnetic quantum number $m_j \in \{-j, -j + 1, \dots, j - 1, j\}$. The three-dimensional noncentrosymmetric bulk Hamiltonian $\hat{H}(\mathbf{k})$, formulated in either the $j = 3/2$ or the $j = 5/2$ representation near the Γ point, is derived from group-theoretical analysis, see Appendix B and Appendix C, as follows:

$$\hat{H}(\mathbf{k}) = \hat{\mathcal{H}}_t(\mathbf{k}) + \hat{\mathcal{H}}_{\text{soc}}(\mathbf{k}), \quad (3)$$

with

$$\hat{\mathcal{H}}_t(\mathbf{k}) = \mathcal{A}_1(\mathbf{k}) \hat{J}_0 + \mathcal{A}_2(\mathbf{k}) \hat{J}_z^2 \quad (4)$$

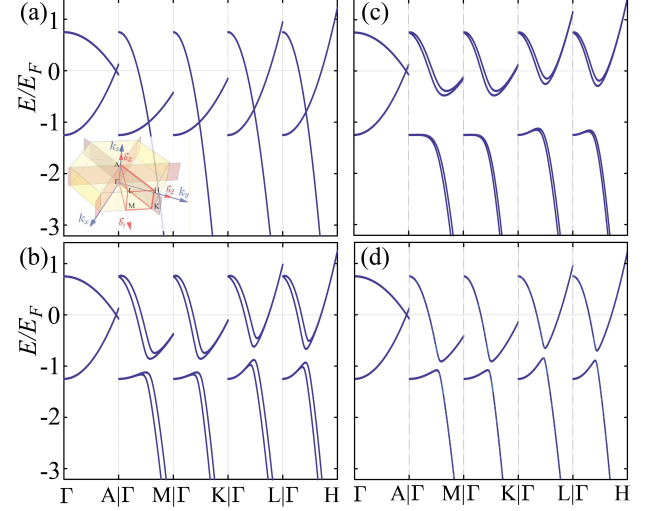


FIG. 1. Bulk band dispersion for $j = 3/2$ electrons near Γ point preserving time-reversal and C_{3v} symmetry, shown for two high-rank spin-orbit coupling configurations from decomposition (a) $A_{1,+} \otimes A_{1,+}$ and (b)–(d) $A_{1,+} \otimes A_{1,+} + E_- \otimes E_-$. Model parameters are (a) $(\mu_2, \alpha_{2,1}, \alpha_{2,2})/E_F = (-1, 1, 1)$, (b) $\gamma_{1,1} = 0.3/E_F$, (c) $\gamma_{1,2} = 0.6/E_F$, and (d) $\gamma_{1,3} = 0.3/E_F$. Other parameters are $(\alpha_{1,1}, \alpha_{1,2})/E_F = (-2, -1)$ and $E_F = \mu_1$. The inset in (a) illustrates Brillouin zone with a trigonal pyramid in a hexagonal setting [78].

where $\hat{\mathcal{H}}_t(-\mathbf{k}) = \hat{\mathcal{H}}_t(\mathbf{k})$ is even-parity including momentum-dependent polynomials $\mathcal{A}_1(\mathbf{k})$ and $\mathcal{A}_2(\mathbf{k})$ representing the kinetic term and the m_j -dependent SOC energy shift, both transforming according to the $A_{1,+} \otimes A_{1,+}$ direct product. Note that in Eq. (4), we keep only the minimal time-reversal-even C_{3v} -allowed kinetic invariants, \hat{J}_0 and \hat{J}_z^2 , which capture the leading band curvature and axial anisotropy near Γ . The remaining even terms, allowed by symmetry, are higher-order (in \mathbf{k} and/or TAM rank). They are listed in Table I. One needs to combine the TAM tensor matrix with the relevant basis polynomial such that the resulting term transforms according to the $A_{1,+}$ irrep. These terms can be included straightforwardly for material-specific modeling. In Eq. (4), the polynomials are defined by

$$\mathcal{A}_i(\mathbf{k}) = \mu_i + \alpha_{i,1}(k_x^2 + k_y^2) + \alpha_{i,2}k_z^2, \quad (5)$$

where $\alpha_{i,1}$ and $\alpha_{i,2}$ specify the in-plane and out-of-plane kinetic energy, respectively, and μ_1 (μ_2) denotes the Fermi energy (m_j -dependent energy shift).

In the following, we illustrate our general analysis for the non-trivial case of $j = 3/2$ electrons, where $\hat{\mathbf{J}}$ are 4×4 matrices. This choice allows us to still obtain analytical results. The same symmetry-based construction applies to other $j > 1/2$ manifolds (including $j = 5/2$); only the algebraic complexity of the explicit matrix expressions increases.

In Eq. (4), when $\mathcal{A}_2(\mathbf{k}) \neq 0$, the fourfold degeneracy of the $j = 3/2$ manifold in $\mathcal{A}_1(\mathbf{k})$ splits into a pair of doubly

Table I. Basis matrices and momentum dependent polynomials transforming according to \mathcal{M}_{3v} gray magnetic group symmetry. $\mathcal{A}_i(\mathbf{k})$ is defined in Eq. (4) and $\mathcal{B}_i(\mathbf{k}) = m_{1,i}k_y(3k_x^2 - k_y^2) + m_{2,i}k_y(3k_x^2 - k_y^2)k_z^2$. Basis polynomial for doublet E_+ is (ϱ_i, ϖ_i) where $\varrho_i = u_{1,i}k_xk_z + u_{2,i}(k_x^2 - k_y^2) + u_{3,i}(k_x^2 - k_y^2)k_z^2 + u_{4,i}[(k_x^2 - k_y^2)^2 - 4k_x^2k_y^2] + u_{5,i}k_xk_z^3$, and $\varpi_i = -u_{1,i}k_yk_z + 2u_{2,i}k_xk_y + 2u_{3,i}k_xk_yk_z^2 - 4u_{4,i}(k_y^2 - k_x^2)k_yk_x - u_{5,i}k_yk_z^3$, where $m_{\nu,i}$ and $u_{\nu,i}$ are material dependent parameters controlling the strength of spin-orbit energy. Leading order of TAM (momenta) in E_+ and A_{2-} are dipolar and quadrupolar (cubic and quadratic), respectively.

	TAM tensor	Polynomials	$j > 1/2$
$A_{1,+}$	\hat{J}_0	$\mathcal{A}_i(\mathbf{k})$	
$A_{1,+}$	$\hat{J}_z^2, \lceil (\hat{J}_x^3 - 3\lceil \hat{J}_x \hat{J}_y^2 \rceil) \hat{J}_z \rceil, \hat{J}_z^4$	$\mathcal{A}_i(\mathbf{k})$	✓
$A_{2,+}$	$\lceil (3\lceil \hat{J}_y \hat{J}_x^2 \rceil - \hat{J}_y^3) \hat{J}_z \rceil$	$k_z(3k_yk_x^2 - k_y^3)$	✓
E_+	$\hat{J}_x^2 - \hat{J}_y^2$	$\varrho_i(\mathbf{k})$	✓
	$2\lceil \hat{J}_x \hat{J}_y \rceil$	$\varpi_i(\mathbf{k})$	✓
E_+	$\lceil \hat{J}_x \hat{J}_z \rceil$	$\varrho_i(\mathbf{k})$	✓
	$\lceil \hat{J}_y \hat{J}_z \rceil$	$-\varpi_i(\mathbf{k})$	✓
E_+	$\lceil \hat{J}_x \hat{J}_z^3 \rceil$	$\varrho_i(\mathbf{k})$	✓
	$\lceil \hat{J}_y \hat{J}_z^3 \rceil$	$-\varpi_i(\mathbf{k})$	✓
$A_{1,-}$	$3\lceil \hat{J}_y \hat{J}_x^2 \rceil - \hat{J}_y^3$	k_z	✓
$A_{1,-}$	$\lceil (3\lceil \hat{J}_y \hat{J}_x^2 \rceil - \hat{J}_y^3) \hat{J}_z \rceil$	k_z	✓
$A_{2,-}$	\hat{J}_z	$\mathcal{B}_i(\mathbf{k})$	
$A_{2,-}$	$\hat{J}_x^3 - 3\lceil \hat{J}_x \hat{J}_y^2 \rceil$	$\mathcal{B}_i(\mathbf{k})$	✓
$A_{2,-}$	\hat{J}_z^3	$\mathcal{B}_i(\mathbf{k})$	✓
E_-	\hat{J}_y	$\Lambda_i(\mathbf{k})$	
	\hat{J}_x	$\Upsilon_i(\mathbf{k})$	
E_-	$\lceil \hat{J}_y \hat{J}_z^2 \rceil$	$\Lambda_i(\mathbf{k})$	✓
	$\lceil \hat{J}_x \hat{J}_z^2 \rceil$	$\Upsilon_i(\mathbf{k})$	✓
E_-	$\lceil \hat{J}_x \hat{J}_y \hat{J}_z \rceil$	$\Lambda_i(\mathbf{k})$	✓
	$\frac{1}{2}\lceil (\hat{J}_y^2 - \hat{J}_x^2) \hat{J}_z \rceil$	$\Upsilon_i(\mathbf{k})$	✓

degenerate energy bands, see Fig. 1(a), given by

$$E_{\text{HM}}(\mathbf{k}) = \mathcal{A}_1(\mathbf{k}) + \frac{9}{4}\mathcal{A}_2(\mathbf{k}), \quad (6)$$

$$E_{\text{LM}}(\mathbf{k}) = \mathcal{A}_1(\mathbf{k}) + \frac{1}{4}\mathcal{A}_2(\mathbf{k}), \quad (7)$$

where the labels “heavy” (HM) and “light” (LM) refer to the band curvature (effective mass) near the Γ point. For a dispersion $E(\mathbf{k})$, the inverse effective-mass tensor is defined as $(m^{-1})_{\nu\nu'}(\Gamma) = [(1/\hbar^2)\partial^2 E(\mathbf{k})/\partial k_\nu \partial k_{\nu'}]|_{\mathbf{k}=\Gamma}$. Both branches are quadratic and anisotropic, and $(m^{-1})_{\nu\nu'}(\Gamma)$ is diagonal. The curvature coefficients are

$$M_{\perp}^{\text{HM}} = \alpha_{1,1} + \frac{9}{4}\alpha_{2,1}, \quad M_z^{\text{HM}} = \alpha_{1,2} + \frac{9}{4}\alpha_{2,2}, \quad (8)$$

$$M_{\perp}^{\text{LM}} = \alpha_{1,1} + \frac{1}{4}\alpha_{2,1}, \quad M_z^{\text{LM}} = \alpha_{1,2} + \frac{1}{4}\alpha_{2,2}. \quad (9)$$

Consequently, the effective masses are $m_{\perp}^{\lambda} = \hbar^2/2M_{\perp}^{\lambda}$ and $m_z^{\lambda} = \hbar^2/2M_z^{\lambda}$ with $\lambda \in \{\text{HM,LM}\}$. Thus, along a given direction the branch is “heavier” (“lighter”) if it has smaller (larger) curvature magnitude, i.e. larger

(smaller) $|m_{\perp,z}^{\lambda}|$. Note that this mass-based labeling is distinct from the energetic ordering of the two branches: their energy separation is $\Delta E(\mathbf{k}) = 2\mathcal{A}_2(\mathbf{k})$, so the sign of $\mathcal{A}_2(\mathbf{k})$ controls which branch lies higher in energy at a given \mathbf{k} .

In Eq. (3), $\hat{\mathcal{H}}_{\text{soc}}(\mathbf{k})$ denotes the odd-parity SOC term present due to broken inversion symmetry, i.e., $\hat{\mathcal{H}}_{\text{soc}}(-\mathbf{k}) = -\hat{\mathcal{H}}_{\text{soc}}(\mathbf{k})$, transforming according to the decomposition $A_{1,+} = E_- \otimes E_-$, given explicitly by

$$\hat{\mathcal{H}}_{\text{soc}}(\mathbf{k}) = \hat{\mathcal{H}}_{\text{MR}}(\mathbf{k}) + \hat{\mathcal{H}}_{\text{HS}}(\mathbf{k}), \quad (10)$$

where $\hat{\mathcal{H}}_{\text{MR}}(\mathbf{k})$ denotes the SOC term constructed from rank-1 (dipolar) basis functions. We call it modified Rashba (MR). It can be written as

$$\hat{\mathcal{H}}_{\text{MR}}(\mathbf{k}) = \Upsilon_1(\mathbf{k})\hat{J}_x + \Lambda_1(\mathbf{k})\hat{J}_y. \quad (11)$$

Additionally, $\hat{\mathcal{H}}_{\text{HS}}(\mathbf{k})$ denotes the contribution from higher-rank multipolar basis functions, given by

$$\hat{\mathcal{H}}_{\text{HS}}(\mathbf{k}) = \hat{\mathcal{H}}_{\text{HS}}^{(1)}(\mathbf{k}) + \hat{\mathcal{H}}_{\text{HS}}^{(2)}(\mathbf{k}), \quad (12)$$

$$\hat{\mathcal{H}}_{\text{HS}}^{(1)}(\mathbf{k}) = \Upsilon_2(\mathbf{k})\lceil \hat{J}_x \hat{J}_z^2 \rceil + \Lambda_2(\mathbf{k})\lceil \hat{J}_y \hat{J}_z^2 \rceil, \quad (13)$$

$$\hat{\mathcal{H}}_{\text{HS}}^{(2)}(\mathbf{k}) = \frac{1}{2}\Upsilon_3(\mathbf{k})\lceil (\hat{J}_y^2 - \hat{J}_x^2) \hat{J}_z \rceil + \Lambda_3(\mathbf{k})\lceil \hat{J}_x \hat{J}_y \hat{J}_z \rceil, \quad (14)$$

where the symmetrization operator for triple and double products is defined by $\lceil \hat{A}\hat{B}\hat{C} \rceil = (1/6)(\hat{A}\hat{B}\hat{C} + \hat{C}\hat{A}\hat{B} + \hat{B}\hat{C}\hat{A} + \hat{C}\hat{B}\hat{A} + \hat{A}\hat{C}\hat{B} + \hat{B}\hat{A}\hat{C})$ and $\lceil \hat{A}\hat{B} \rceil = (1/2)(\hat{A}\hat{B} + \hat{B}\hat{A})$, respectively. Both $\Upsilon_i(\mathbf{k})$ and $\Lambda_i(\mathbf{k})$, which appear in Eqs. (11)–(14), are odd functions of momentum. They can be written as polynomials in \mathbf{k} up to the fifth order as

$$\begin{aligned} \Lambda_i(\mathbf{k}) = & \gamma_{1,i}k_x + \gamma_{2,i}(k_x^2 - k_y^2)k_z + \gamma_{3,i}k_xk_z^2 \\ & + \gamma_{4,i}(k_x^5 - 10k_x^3k_y^2 + 5k_xk_y^4), \end{aligned} \quad (15)$$

$$\begin{aligned} \Upsilon_i(\mathbf{k}) = & -\gamma_{1,i}k_y + \gamma_{2,i}(2k_xk_yk_z) - \gamma_{3,i}k_yk_z^2 \\ & + \gamma_{4,i}(k_y^5 - 10k_x^2k_y^3 + 5k_x^4k_y), \end{aligned} \quad (16)$$

where $\gamma_{1,i}$ defines the SOC linear in momentum and $\gamma_{2(3),i}$, and $\gamma_{4,i}$ are cubic and quintic in momentum, respectively. Importantly, $\hat{\mathcal{H}}_{\text{HS}}(\mathbf{k})$ is exclusive for high TAM. This is because the squared angular momentum operators do not result in the identity matrix, i.e., $\hat{J}_i^2 \neq 1$, unlike for the $j = 1/2$ electrons. Note that $\hat{\mathcal{H}}_{\text{HS}}^{(1)}(\mathbf{k})$ and $\hat{\mathcal{H}}_{\text{MR}}(\mathbf{k})$ are identical in the $j = 1/2$ basis. They reduce to the conventional Rashba SOC up to linear momenta $\hat{\mathcal{H}}_{1/2}(\mathbf{k}) = k_x\hat{\sigma}_y - k_y\hat{\sigma}_x$, and $\hat{\mathcal{H}}_{\text{HS}}^{(2)}(\mathbf{k})$ vanishes.

The analogue of the spin-texture vector in the $j = 1/2$ basis is the total-angular-momentum texture vector,

$$\mathbf{J}_n(\mathbf{k}) = (\langle \hat{J}_x \rangle_{n\mathbf{k}}, \langle \hat{J}_y \rangle_{n\mathbf{k}}, \langle \hat{J}_z \rangle_{n\mathbf{k}}), \quad (17)$$

where $\langle \hat{J}_i \rangle_{n\mathbf{k}} = \langle u_{n\mathbf{k}} | \hat{J}_i | u_{n\mathbf{k}} \rangle$ denotes the expectation value of the i -th component of the total angular-momentum operator in the Bloch eigenstate $|u_{n\mathbf{k}}\rangle$ of

band n at momentum \mathbf{k} . If $\mathcal{A}_2(\mathbf{k}) \neq 0$, we obtain a constant out-of-plane TAM texture, i.e., $\mathbf{J}_{\text{HM}}(\mathbf{k}) = (0, 0, \pm 3/2)$ and $\mathbf{J}_{\text{LM}}(\mathbf{k}) = (0, 0, \pm 1/2)$. The net TAM texture is zero since the $A_{1+} \otimes A_{1+}$ decomposition is symmetric under time-reversal and parity operations.

III. SYMMETRY PROPERTIES

The full Hamiltonian in Eq. (3) is invariant under the time-reversal operation, $\hat{\mathcal{T}}\hat{H}(\mathbf{k})\hat{\mathcal{T}}^\dagger = \hat{H}(-\mathbf{k})$, where $\hat{\mathcal{T}} = \exp(-i\pi\hat{J}_y)\mathcal{K}$ is the anti-unitary time-reversal operator with \mathcal{K} denoting complex conjugation. Additionally, $\hat{H}(\mathbf{k})$ transforms according to the $A_{1,+}$ irrep of the \mathcal{M}_{3v} magnetic point group, as implied by the covariant symmetry condition $\hat{H}(R^{-1}\mathbf{k}) = \hat{g}\hat{H}(\mathbf{k})\hat{g}^\dagger$, where $\hat{g} \in \{E, 2C_{3z}, 3\sigma_v, 2TC_{3z}, 3T\sigma_v, T\}$ represents the symmetry elements, including the identity operator E , the three-fold rotation around the z -axis C_{3z} , the mirror reflections σ_v , and their combinations with time-reversal symmetry T . Here, R is a 3×3 orthogonal rotation matrix in momentum space. Under threefold rotation and mirror reflection, TAM and momentum transform as follows:

$$R_{3z}^{-1}\mathbf{k} = \begin{pmatrix} \frac{-1}{2} & \frac{-\sqrt{3}}{2} & 0 \\ \frac{\sqrt{3}}{2} & \frac{-1}{2} & 0 \\ 0 & 0 & 1 \end{pmatrix} \mathbf{k}, \quad (18)$$

$$\sigma_{v_1}^{-1}\mathbf{k} = \begin{pmatrix} +1 & 0 & 0 \\ 0 & -1 & 0 \\ 0 & 0 & +1 \end{pmatrix} \mathbf{k}, \quad (19)$$

$$\hat{C}_{3z}\hat{\mathbf{J}}\hat{C}_{3z}^{-1} = \begin{pmatrix} \frac{-1}{2} & \frac{\sqrt{3}}{2} & 0 \\ \frac{-\sqrt{3}}{2} & \frac{-1}{2} & 0 \\ 0 & 0 & 1 \end{pmatrix} \hat{\mathbf{J}}, \quad (20)$$

$$\hat{M}_1\hat{\mathbf{J}}\hat{M}_1^{-1} = \begin{pmatrix} -1 & 0 & 0 \\ 0 & +1 & 0 \\ 0 & 0 & -1 \end{pmatrix} \hat{\mathbf{J}}, \quad (21)$$

where $\hat{C}_{3z} = \exp(-2\pi i \hat{J}_z/3)$ and $\hat{M}_1 = \exp(-i\pi\hat{J}_y)$ denotes the matrix form in $j \in \{3/2, 5/2\}$ basis for three-fold rotation and mirror reflection operators, respectively. Under time-reversal operation, both the TAM vector $\hat{\mathbf{J}}$ and the momentum vector \mathbf{k} reverse sign, i.e., $\hat{\mathbf{J}} \rightarrow -\hat{\mathbf{J}}$ and $\mathbf{k} \rightarrow -\mathbf{k}$. The symmetry-allowed terms in the Hamiltonian $\hat{H}(\mathbf{k})$ are summarized in Table I, where we list all allowed TAM and momentum bases that transform properly under \mathcal{M}_{3v} . Note that we adopt the conventions of Ref. [79], in which mirror reflection symmetry implies $k_y \rightarrow -k_y$. However, for the trigonal P31m space group, as in PtBi₂, the mirror planes are oriented differently so that the A_{2-} basis function is rotated to $k_x(3k_y^2 - k_x^2)$ [67].

IV. BAND BASIS REPRESENTATION

Without loss of generality, we represent Eq. (3) in the eigenbasis of $\hat{\mathcal{H}}_t(\mathbf{k})$, where the magnetic quantum number m_j serves as a proper band index, i.e., $\hat{V}^\dagger \hat{\mathcal{H}}_t(\mathbf{k}) \hat{V} = \text{diag}(E_{\text{LB}}(\mathbf{k}), E_{\text{HB}}(\mathbf{k}))$. In this basis defined by

$$\hat{V} = \begin{pmatrix} 0 & 0 & 0 & 1 \\ 0 & 1 & 0 & 0 \\ 1 & 0 & 0 & 0 \\ 0 & 0 & 1 & 0 \end{pmatrix}, \quad (22)$$

the full SOC Hamiltonian takes the form

$$\begin{aligned} \hat{\mathcal{H}}(\mathbf{k}) &= \hat{V}^\dagger \hat{H}(\mathbf{k}) \hat{V} \\ &= \begin{pmatrix} \hat{H}_{\text{LM}}(\mathbf{k}) & \hat{C}(\mathbf{k}) \\ [\hat{C}(\mathbf{k})]^\dagger & \hat{H}_{\text{HM}}(\mathbf{k}) \end{pmatrix} \\ &\equiv \hat{H}_0(\mathbf{k}) + \hat{V}_{\text{off}}(\mathbf{k}), \end{aligned} \quad (23)$$

where the first term is block-diagonal $\hat{H}_0(\mathbf{k}) = \text{diag}(\hat{H}_{\text{LM}}(\mathbf{k}), \hat{H}_{\text{HM}}(\mathbf{k}))$ with $\hat{H}_{\text{HM}} = E_{\text{HM}}(\mathbf{k})\hat{\sigma}_0$, and \hat{V}_{off} is the off-diagonal coupling part denoting the SOC coupling between light and heavy bands, namely interband SOC. These terms explicitly read

$$\hat{H}_{\text{LM}}(\mathbf{k}) = \begin{pmatrix} E_{\text{LM}}(\mathbf{k}) & g(\mathbf{k}) \\ [g(\mathbf{k})]^\dagger & E_{\text{LM}}(\mathbf{k}) \end{pmatrix}, \quad (24)$$

$$\hat{V}_{\text{off}}(\mathbf{k}) = \begin{pmatrix} 0 & \hat{C}(\mathbf{k}) \\ [\hat{C}(\mathbf{k})]^\dagger & 0 \end{pmatrix}, \quad (25)$$

where the intraband SOC in the LM sector can be written as

$$g(\mathbf{k}) = \mathcal{Z}_1^+(\mathbf{k}) + \frac{1}{4}\mathcal{Z}_2^+(\mathbf{k}) \quad (26)$$

with $\mathcal{Z}_\nu^\pm(\mathbf{k}) = \Upsilon_\nu(\mathbf{k}) \pm i\Lambda_\nu(\mathbf{k})$. The off-diagonal sector \hat{C} in Eq. (25) is given by

$$\hat{C}(\mathbf{k}) = \begin{pmatrix} \mathcal{F}(\mathbf{k}) & \mathcal{C}(\mathbf{k}) \\ -[\mathcal{C}(\mathbf{k})]^* & [\mathcal{F}(\mathbf{k})]^* \end{pmatrix}, \quad (27)$$

where the interband SOC elements read

$$\mathcal{F}(\mathbf{k}) = \frac{\sqrt{3}}{2}[\mathcal{Z}_1^-(\mathbf{k}) + \frac{5}{4}\mathcal{Z}_2^-(\mathbf{k})], \quad (28)$$

$$\mathcal{C}(\mathbf{k}) = -\frac{\sqrt{3}}{4}\mathcal{Z}_3^-(\mathbf{k}). \quad (29)$$

The spectrum of $\hat{\mathcal{H}}(\mathbf{k})$ is analytically solvable as

$$E_{1,\pm}(\mathbf{k}) = \pm \frac{\mathcal{D}(\mathbf{k}) - |g(\mathbf{k})|}{2}, \quad (30)$$

$$E_{2,\pm}(\mathbf{k}) = \pm \frac{\mathcal{D}(\mathbf{k}) + |g(\mathbf{k})|}{2}, \quad (31)$$

where $\mathcal{D} = \sqrt{|g|^2 + 4A}$, $A \equiv |\mathcal{C}|^2 + |\mathcal{F}|^2$ denotes the full interband SOC, and $|A| = \sqrt{AA^*}$. For brevity, the \mathbf{k} dependence is omitted henceforth. Importantly, the spectrum reduces to the conventional spin splitting $E_{2,\pm}(\mathbf{k}) = \pm|g|$ for $j = 1/2$ electrons while $E_{1,\pm}(\mathbf{k})$ vanishes. This is because the interband SOC is absent in a two band model, i.e., $\mathcal{C} = \mathcal{F} = 0$.

Generally, the analysis of the spectrum of $\hat{\mathcal{H}}_{\text{soc}}$ can be summarized as follows. A pure modified Rashba term $\hat{\mathcal{H}}_{\text{MR}}$ emerges for $\mathcal{C} = 0$, $\mathcal{F} = (\sqrt{3}/2)\mathcal{Z}_1^-$, and $g = \mathcal{Z}_1^+$ so that both intraband SOC (g) and interband SOC (\mathcal{F}) are present, see Fig. 1(b). The positive branches of the spectrum are $(1/2)\sqrt{|g|^2 + 3|\mathcal{Z}_1^-|^2 \pm |g|}$, implying that the interband SOC results in an additional monotonic splitting. The doubly degeneracy along the $\Gamma - A$ path is protected by the \mathcal{M}_{3v} space group since Υ_1 and Λ_1 are independent of k_z . However, it can be split when an additional SOC channel like $A_{1,-} \otimes A_{1,-}$ is included in the SOC Hamiltonian. Furthermore, a pure $\hat{\mathcal{H}}_{\text{HS}}^{(1)}$ emerges for $\mathcal{C} = 0$ and $\mathcal{F} = (5\sqrt{3}/8)\mathcal{Z}_2^-$, similarly to $\hat{\mathcal{H}}_{\text{MR}}$ but with an effective larger interband amplitude, see Fig. 1(c). Subsequently \mathcal{D} increases as $\sqrt{|g|^2 + (75/64)|\mathcal{Z}_2^-|^2}$ and both positive branches shift slightly upward relative to $\hat{\mathcal{H}}_{\text{MR}}$. A pure $\hat{\mathcal{H}}_{\text{HS}}^{(2)}$ emerges for $g = \mathcal{F} = 0$ and $\mathcal{C} = -(\sqrt{3}/4)\mathcal{Z}_3^-$, leaving only interband SOC. Then, $\mathcal{D} = 2|\mathcal{C}|$ and the spectrum collapses into a pair of doubly degenerate levels at $E_{\pm,\pm} \in \{\pm|\mathcal{C}|, \pm|\mathcal{C}|\}$ (no interband spin splitting), as depicted in Fig. 1(d).

The spin splittings for the intraband (“intra”) and interband (“inter”) branches are observable and given by

$$\Delta E_{\text{intra}}^{\pm} = \mathcal{D} \pm |g|, \quad (32)$$

$$\Delta E_{\text{inter}} = \mathcal{D}. \quad (33)$$

In the weak-hybridization regime $A \ll |g|$ (compared to the intraband SOC), \mathcal{D} becomes

$$\mathcal{D} \approx |g| + \frac{2A}{|g|} - \frac{2A^2}{|g|^3} + O(A^3), \quad (34)$$

giving rise to a weakly growing splitting with hybridization in the energy bands

$$\Delta E_{\text{intra}}^+ \approx 2|g| + \frac{2A}{|g|} - \frac{2A^2}{|g|^3} + O(A^3), \quad (35)$$

$$\Delta E_{\text{intra}}^- \approx \frac{2A}{|g|} - \frac{2A^2}{|g|^3} + O(A^3). \quad (36)$$

However, in the strong hybridization limit $A \gg |g|$, we obtain $\mathcal{D} \approx 2\sqrt{A} + |g|^2/4\sqrt{A} + O(|g|^4)$. Then, the band splitting is dominated by interband SOC, i.e., $\Delta E_{\text{intra}}^{\pm} \approx 2\sqrt{A} \pm |g|$.

The magnitude of the anisotropic spin-splitting for the $j = 1/2$ and $j = 3/2$ states close to the Γ point are illustrated in Fig. 2. The SOC Hamiltonian includes terms up to fifth order in momentum. We plot the contributions

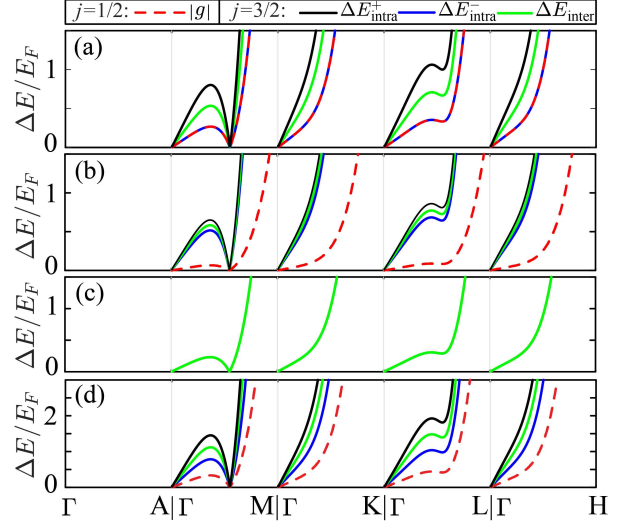


FIG. 2. Magnitude of $E_- \otimes E_-$ intraband and interband spin splittings for $j = 1/2$ and $j = 3/2$ electrons near the bulk Γ point, evaluated along a trigonal-pyramidal path in the hexagonal Brillouin zone. Model parameters are fixed to $\gamma_{1,i} = \gamma_{2,i} = \gamma_{3,i} = \gamma_{4,i} = 0.5 E_F$. (a) Pure modified Rashba $\hat{\mathcal{H}}_{\text{MR}}$ with $i = 1$, (b) pure $\hat{\mathcal{H}}_{\text{HS}}^{(1)}$ with $i = 2$, (c) pure high-spin term $\hat{\mathcal{H}}_{\text{HS}}^{(2)}$ with $i = 3$, and (d) full SOC $\sum_{i=1}^3 \hat{\mathcal{H}}_i$ with $\hat{\mathcal{H}}_i$ denoting pure terms in panels (a)–(c).

from the modified Rashba channel $\hat{\mathcal{H}}_{\text{MR}}$ in Fig. 2(a), the high-rank SOC channels $\hat{\mathcal{H}}_{\text{HS}}^{(1,2)}$ in Figs. 2(b) and 2(c), and the full term $\hat{\mathcal{H}}_{\text{soc}}$ is illustrated in Fig. 2(d). Notably, the splitting in the $j = 3/2$ bands ($\Delta E_{\text{intra}}^+$) exceeds that of the $j = 1/2$ states; compare the black curves in Figs. 2(a) and 2(b). Although the splitting generated by $\hat{\mathcal{H}}_{\text{HS}}^{(2)}$ is purely of interband character [see Fig. 2(c)], its magnitude is smaller than in $\hat{\mathcal{H}}_{\text{MR}}$, and its higher rank counterpart $\hat{\mathcal{H}}_{\text{HS}}^{(1)}$. Importantly, along $\Gamma - M$, the splitting from $\hat{\mathcal{H}}_{\text{MR}}$ and $\hat{\mathcal{H}}_{\text{HS}}^{(1)}$ vanishes at a critical momentum \mathbf{k}_c and afterward rises sharply, due to the dominant fifth-order terms, see Figs. 2(a) and 2(b). This can be verified analytically by setting $k_y = k_x/\sqrt{3}$ and $k_z = 0$, then, the component of splitting becomes $\Lambda_1 \propto -k_x(4k_x^2 - 3)(4k_x^2 + 3)$ and $\Upsilon_1 \propto -\Lambda_1$. Therefore, Λ_1 vanishes at $k_x = \pm\sqrt{3}/2$. Thus, the splitting vanishes at $\mathbf{k}_c = (k_x, k_y) = (\sqrt{3}/2, 1/2)$. In addition, along $\Gamma - A$, splitting is forbidden by the \mathcal{M}_{3v} point group in the $E_- \otimes E_-$ decomposition. Note that in Fig. 2(a), the $j = 1/2$ splitting matches that of the $j = 3/2$ band $E_{1,\pm}(\mathbf{k})$ because $A = 3/4|g|^2$ and $\mathcal{D} = 2|g|$, yielding $\Delta E_{\text{intra}}^- = \mathcal{D} - |g| = |g|$.

Let us emphasize that interband SOC, beyond the familiar intraband Rashba splitting, has been directly observed in Bi-based surface alloys, where hybridization between Rashba-split bands strongly reshapes the dispersion and spin-orbital character of surface states [80, 81]. It leaves clear fingerprints in optical responses—for example, the suppression of interband absorption in the

persistent spin-helix regime of Rashba–Dresselhaus systems. Therefore, it serves as a sensitive probe of engineered SOC [82]. These observations motivate effective models that explicitly include interband SOC terms to faithfully capture spin-orbit-entangled bands in low-dimensional electron systems [83].

V. WINDING OF THE TOTAL-ANGULAR-MOMENTUM FIELD

A pure modified Rashba term $\hat{\mathcal{H}}_{\text{MR}}$ yields an in-plane TAM texture whose winding number is determined by the momentum-polynomial order. In this case, we find that the TAM texture for a given j is independent of m_j and, in fact, identical for all multiplets considered, $W_{j,m_j} = W$ where $j \in \{1/2, 3/2, 5/2\}$ and $m_j \in [-j, \dots, j]$. Therefore, the light and heavy bands share the same TAM texture. Interestingly, once the multipolar terms are included, this universality is lost and the heavy and light bands acquire different winding numbers. This can be understood as a consequence of the multipolar components associated with $|m_j| > 1/2$, which transform under a different symmetry than the dipolar Rashba term and therefore reshape the texture. To show this, we first discuss the TAM vorticity phase diagram for the modified Rashba term $\hat{\mathcal{H}}_{\text{MR}}$ including momentum-dependent contributions up to fifth order. This serves as a reference against which we compare the effects of the multipolar terms.

Importantly, in the C_{3v} point group symmetry, the z -axis is fixed by symmetry as the unique principal C_3 rotation axis of the crystal, with all mirror planes containing this axis. Accordingly, the vorticity is defined as the winding of the in-plane (i.e., perpendicular-to- z) TAM texture along closed loops taken in planes normal to this symmetry axis. Any other sample orientation is handled by a coordinate rotation aligning z with the crystal's C_3 axis. Moreover, C_{3v} and T symmetries constrain the out-of-plane TAM component to be momentum independent and forbids symmetry-allowed terms of the form $k_z \hat{J}_z$. Therefore, the reciprocal-space Skyrmion number is trivial. In this case, a 2D in-plane winding number can be nontrivial where k_z is treated as a constant.

A. TAM-texture for modified Rashba term $\hat{\mathcal{H}}_{\text{MR}}$

We assume $j = 3/2$ and obtain the winding number of the TAM field in reciprocal space. $\hat{\mathcal{H}}_{\text{MR}}$ exhibits an in-plane TAM texture (the out-of-plane TAM texture is vanishing) given by

$$\mathbf{J}_n(\mathbf{k}) = \frac{n}{\sqrt{[\Lambda_1(\mathbf{k})]^2 + [\Upsilon_1(\mathbf{k})]^2}} \begin{pmatrix} \Upsilon_1(\mathbf{k}) \\ \Lambda_1(\mathbf{k}) \\ 0 \end{pmatrix}, \quad (37)$$

where $n = m_j \in \{\pm 1/2, \pm 3/2\}$ is the band index and the helicity of each band is determined by the sign of m_j : $\text{sgn}(m_j) = +1$ (-1) corresponds to clockwise (anticlockwise) winding. $\mathbf{J}_{m_j}(-\mathbf{k}) = -\mathbf{J}_{m_j}(\mathbf{k})$ is odd in momentum because both $\Upsilon_1(\mathbf{k})$ and $\Lambda_1(\mathbf{k})$ are odd and fulfills the helical property $\mathbf{J}_{-m_j}(\mathbf{k}) = -\mathbf{J}_{m_j}(\mathbf{k})$. $\hat{\mathcal{H}}_{\text{MR}}$ implies that $(g, \mathcal{F}, \mathcal{C}) = (\mathcal{Z}_1^+, \sqrt{3}/2\mathcal{Z}_1^-, 0)$. In this case, the dispersion in Eqs. (30) and (31) becomes $E_{\pm 1/2} = \mu_1 \pm (1/2)|\mathcal{Z}_1^+|$ and $E_{\pm 3/2} = \mu_1 \pm (3/2)|\mathcal{Z}_1^+|$ where $|\mathcal{Z}_1^+| = \sqrt{\Lambda_1^2 + \Upsilon_1^2}$.

The winding number of the in-plane TAM texture in band n around a closed contour \mathcal{C} in momentum space is defined as $W_n = (1/2\pi) \oint_{\mathcal{C}} d\varphi_{n,\mathbf{k}}$, where $\varphi_{n,\mathbf{k}}$ is the local TAM angle in the (J_x, J_y) plane. Equivalently, one may introduce the complex TAM field $\mathcal{Z}_n \equiv \langle \hat{J}_x \rangle_{n\mathbf{k}} + i \langle \hat{J}_y \rangle_{n\mathbf{k}}$, whose phase satisfies $\varphi_{n,\mathbf{k}(t)} = \arg(\mathcal{Z}_n(t, \mathbf{q}))$ so that the winding number can be expressed in the general complex-analysis form

$$W_n(\mathbf{q}) = \frac{1}{2\pi i} \oint_{|t|=1} \frac{\partial_t \mathcal{Z}_n(t, \mathbf{q})}{\mathcal{Z}_n(t, \mathbf{q})} dt = \sum_i N_i(\mathbf{q}) - \sum_i M_i(\mathbf{q}), \quad (38)$$

where $N_i(\mathbf{q})$ and $M_i(\mathbf{q})$ denote, respectively, the multiplicities of zeros and poles of $\mathcal{Z}_n(t, \mathbf{q})$ enclosed by the contour. $W_n(\mathbf{q})$ is proportional to the difference of total number of zeros $N_i(\mathbf{q})$ and poles $M_i(\mathbf{q})$ of $\mathcal{Z}_n(t, \mathbf{q})$ inside the unit circle. The explicit form for the complex map can be written as

$$\begin{aligned} \mathcal{Z}_n(t, \mathbf{q}) &= \Upsilon_1(t, \mathbf{q}) + i\Lambda_1(t, \mathbf{q}) \\ &= (q_1 + q_2 t_\varphi^3 + q_3 t_\varphi^6)/t_\varphi, \end{aligned} \quad (39)$$

where $\mathbf{q} = (q_1, q_2, q_3)$ is a vector of material dependent constants defined by $q_1 \equiv (\gamma_{1,1} + \gamma_{3,1} k_z^2)|\mathbf{k}_\perp|$, $q_2 \equiv \gamma_{2,1} |\mathbf{k}_\perp|^2 k_z$, $q_3 \equiv \gamma_{4,1} |\mathbf{k}_\perp|^5$, $|\mathbf{k}_\perp| = \sqrt{k_x^2 + k_y^2}$, and $t_\varphi = \exp(-i\varphi)$ depends on polar angle with radius $|t| = 1$. Equation (39) has a simple pole at $t_\varphi = 0$ and six zeros in the numerators obtained from $q_1 + q_2 t_\varphi^3 + q_3 t_\varphi^6 = 0$, where the solutions are $t_\varphi \in \{t_1, t_2\}$ with t_1 (t_2) denoting fourfold (twofold) degenerate roots given by $t_1 = \sqrt[3]{f_\pm(\mathbf{q})/2}$ ($t_2 = (-1)^{2/3} t_1$), where $f_\pm(\mathbf{q}) = -q_2/q_3 \pm [(q_2^2 - 4q_1 q_3)^{1/2}/q_3]$. Since only one pole locates inside the unit circle, this results in $\sum_i M_i(\mathbf{q}) = 1$. In this case, the total number of zeros located inside the loop $|t_\varphi| < 1$ contribute in winding number given by

$$W_n(\mathbf{q}) = \sum_i N_i(\mathbf{q}) - 1, \quad (40)$$

where the solutions of inequalities $t_1 t_1^* < 1$ and $t_2 t_2^* < 1$ defines unique regions of $W_n(\mathbf{q})$.

The outcome is presented in the generic 3D phase diagram in Fig. 3(a). A two-dimensional (2D) slice of the phase diagram at $q_3 = 0.5$ is shown in Fig. 3(b). There

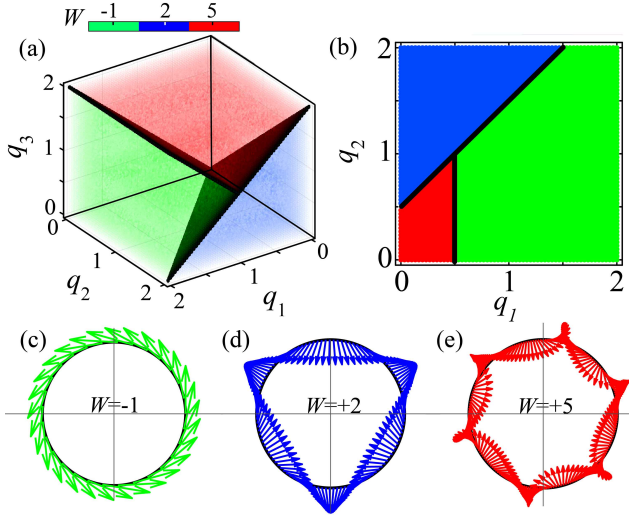


FIG. 3. Phase diagrams of total-angular-momentum vorticity as function of (a) $\mathbf{q} = (q_1, q_2, q_3)$ and (b) $\mathbf{q} = (q_1, q_2, 0.5)$. Polar plots of the j texture for (c) single winding, $W = -1$, at $\mathbf{q} = (1.5, 0, 0.5)$; (d) twofold winding, $W = 2$, at $\mathbf{q} = (0.5, 1.5, 0.5)$; and (e) fivefold winding, $W = 5$, at $\mathbf{q} = (0.2, 0.2, 0.5)$. The color bar indicates the winding number. Black planes and lines in panels (a) and (b) denote boundaries of regions with different winding number.

are three distinct phases, where the TAM texture exhibits the conventional Rashba vortex (green). In this case, the TAM texture winds once around the origin, as illustrated in its polar form in Fig. 3(c). The other regions correspond to unconventional vortices, where the TAM texture exhibits twofold and fivefold windings, marked in blue and red in Figs. 3(d) and 3(e), respectively. The black surfaces indicate the phase boundaries, obtained from the conditions $t_1 t_1^* = 1$ and $t_2 t_2^* = 1$, where the zeros lie on the circumference of the unit circle.

Importantly, in photoemission spectroscopy, the signature of the fivefold winding can be detected as (i) the warping of constant-energy contours near the Fermi energy and (ii) nontrivial TAM winding around the Γ point, either on a two-dimensional surface or in the three-dimensional bulk [84, 85]. In the latter case, larger constant-energy contours become accessible when higher-energy photons are incident on the sample or the chemical potential is changed.

In Fig. 4, we show constant-energy contours of the solutions $E_{-1/2}(\mathbf{k}_\perp) = E_c/\mu_1$ for $E_c/\mu_1 \in [-1, 1]$, for a mixture of SOC terms together with the corresponding TAM texture in the Γ - M - K plane denoted by momentum $\mathbf{k}_\perp \equiv (k_x, k_y, 0)$. When a linear-quintic mixture of SOC is dominant, the dispersion takes the form

$$E_{n,\pm} = \mu_1 \pm n |\mathbf{k}_\perp| \mathcal{G}(\varphi), \quad (41)$$

where $\mathcal{G}(\varphi)$ denotes the angle dependent part of spin split

Table II. Winding of total-angular-momentum texture for pure odd-parity spin-orbit coupling terms $E_- \otimes E_-$ up to fifth order of momentum preserving time-reversal and C_{3v} point group symmetries. Coefficients are $v_{1,3,4} = \text{sgn}(\gamma_{1(3)[4],1})$ and $v_2 = \text{sgn}(k_z \gamma_{2,1})$.

$\neq 0$	\mathbf{k}	$\mathbf{J}_n(\varphi)$	$ W_n $
$\gamma_{1,1}$	Linear	$v_1 \mathbf{e}_\varphi$	1
$\gamma_{2,1}$	Cubic	$v_2 \sin(3\varphi) \mathbf{e}_r + v_2 \cos(3\varphi) \mathbf{e}_\varphi$	2
$\gamma_{3,1}$	Cubic	$v_3 \mathbf{e}_\varphi$	1
$\gamma_{4,1}$	Quintic	$v_4 \sin(6\varphi) \mathbf{e}_r + v_4 \cos(6\varphi) \mathbf{e}_\varphi$	5

dispersion given by

$$\mathcal{G}(\varphi) = \sqrt{\gamma_{1,1}^2 + \gamma_{4,1}^2 |\mathbf{k}_\perp|^8 + 2\gamma_{1,1}\gamma_{4,1} |\mathbf{k}_\perp|^4 \cos(6\varphi)}. \quad (42)$$

It develops hexafoil energy contours for $E_c \geq \pm\mu_1$ due to the $\cos(6\varphi)$, shown in Fig. 4(a). Energy contours are distributed as a central circular pocket surrounded by six lobes. These contours evolve from an almost circular contour at $E \approx E_F$ into a concave hexagon. This can be understood that in the vicinity of the Γ point (i.e., for $|\mathbf{k}_\perp| \ll 1$), the linear SOC term $\propto \mathbf{k}_\perp$ dominates over the quintic term $\propto |\mathbf{k}_\perp|^5$, yielding nearly circular constant-energy contours. In this case, the TAM texture exhibits a conventional helix, see green arrows in Fig. 4(a). Note that the TAM texture of a pure linear $\gamma_{1,1}$ (cubic $\gamma_{3,1}$) SOC has a polar dependence while cubic $\gamma_{2,1}$ and quintic $\gamma_{4,1}$ has an additional radial part, as listed in Table II.

At larger momenta ($|\mathbf{k}_\perp| \gtrsim 1$), the fifth-order SOC becomes dominant and the contours evolve into a concave hexagon. For $E > E_c$, the central pocket disappears and the six lobes merge into a simple hexagon signaling a highly suppressed Rashba contribution. Interestingly, the TAM texture undergoes a nontrivial transition away from the Γ point exhibiting quintic vortex, as illustrated by red arrows in Fig. 4(a). The region with a conventional TAM vortex, characterized by $W_n(|\mathbf{k}_\perp|) = -1$, is separated from the quintic vorticity phase, $W_n(|\mathbf{k}_\perp|) = 5$, by a phase transition boundary, shown as a solid yellow line in Fig. 4(a), across which the winding number undergoes a drastic jump.

The dependence of the winding number on the in-plane momentum can be understood as follows. When a linear-quintic SOC is favored, the zeros of the complex map $\mathcal{Z}_n(t) = 0$ are determined by $\mathcal{Z}_n(t) = \gamma_{1,1} + \gamma_{4,1} |\mathbf{k}_\perp| t^6$. Thus, for given parameter values $\gamma_{1,1}$ and $\gamma_{4,1}$, the TAM vortex depends on the magnitude of $|\mathbf{k}_\perp|$. Even if the fifth-order coefficient is weak, its effect can be enhanced at $|\mathbf{k}_\perp| > 1$, resulting in a hexafoil SOC with a quintic TAM vortex. We note that, for pure modified Rashba SOC, the winding number does not depend on the in-plane momentum.

Up to the rank-1 (dipolar) correction, the SOC energy takes the form

$$\mathcal{H}_{\text{SOC}}(\mathbf{k}) = \hat{\mathcal{H}}_{\text{MR}} + \mathcal{B}_1(\mathbf{k}) \hat{J}_z, \quad (43)$$

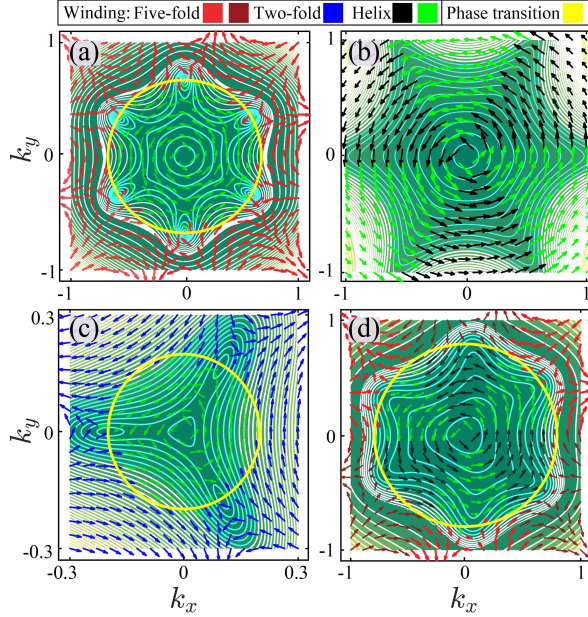


FIG. 4. Two-dimensional constant-energy contours with TAM texture in $j = 3/2$ basis for light-mass band, i.e., $|3/2, -1/2\rangle$. (a) Linear-quintic mixture $E_- \otimes E_-$ with $\gamma_{1,1}/E_F = 0.3$ and $\gamma_{4,1}/E_F = 1.5$, (b) linear-cubic mixture $A_{2,-} \otimes A_{2,-} + E_- \otimes E_-$ for slice $k_z = 0.5$ with $\gamma_{1,1}/E_F = 1$, $m_{1,1}/E_F = 1.5$, and $m_{2,1}/E_F = 1.2$, (c) linear-cubic mixture $E_- \otimes E_-$ with $\gamma_{1,1}/E_F = 0.3$ and $\gamma_{2,1}/E_F = 1.5$, and (d) full term with $\gamma_{\nu,1}/E_F = m_{2,1}/E_F = 0.5$ for $\nu \in \{1, 2, 3\}$, $m_{1,1}/E_F = 1$ and $k_z = 1$. The yellow solid circles denote the phase transition boundaries where the winding changes. The out-of-plane component of TAM texture is marked in dark and light colors. The heavy-mass bands carry similar information. for other helical energy branch $W \rightarrow -W$. Other parameters are set to zero.

where the second term arises from the $A_{2,-} \otimes A_{2,-}$ decomposition, with $\mathcal{B}_1(\mathbf{k})$ and \hat{J}_z providing the momentum and TAM basis functions, respectively, each transforming according to the $A_{2,-}$ irrep and the momentum basis takes the form

$$\mathcal{B}_1(\mathbf{k}) = m_{1,1}k_y(3k_x^2 - k_y^2) + m_{2,1}k_y(3k_x^2 - k_y^2)k_z^2, \quad (44)$$

where $m_{1(2),1}$ is a material-dependent coefficient that sets the strength of the axial Zeeman-type SOC term. Note that, after projecting Eq. (43) onto the effective spin-1/2 sector, it reduces to the familiar hexagonal-warping SOC of the surface states in the topological insulator Bi_2Te_3 [22, 84].

The leading order in $A_{2,-} \otimes A_{2,-}$ decomposition gives rise to an out-of-plane spin texture. Either with $\gamma_{1,1}, m_1 \neq 0$ or $\gamma_{1,1}, \gamma_{2,1} \neq 0$ hexagonal and trigonal warping emerge [22, 86], as shown in Fig. 4(b) and Fig. 4(c), respectively. The former (latter) SOC yields both in-plane and out-of-plane (a purely in-plane) TAM texture. Importantly, the hexagonal warping exhibits conventional TAM vortex $W_n(k_z) = -1$ in the entire Brillouin zone (2D surface or 3D bulk). However, in the

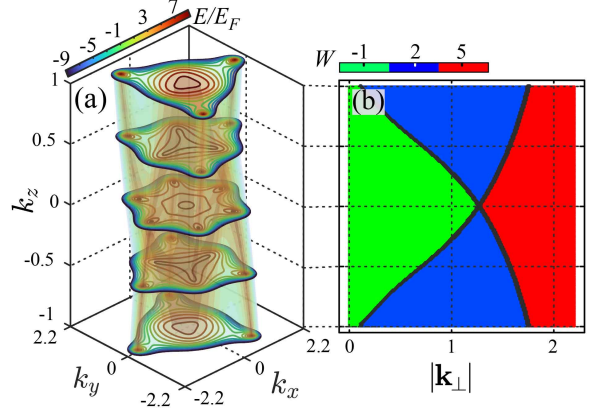


FIG. 5. (a) Three-dimensional bulk spectrum with constant-energy contours and (b) corresponding vorticity phase diagram. Both panels are evaluated for the light mass band with positive helicity, i.e., $|3/2, -1/2\rangle$. Model parameters: $(\gamma_{1,1}, \gamma_{2,1}, \gamma_{3,1}, \gamma_{4,1})/E_F = (-0.5, -1, 0.4, 0.2)$ and $|\mathbf{k}_\perp| = (k_x^2 + k_y^2)^{1/2}$. In panel (a), the constant-energy contours are taken in the range $E/E_F \in [-1, 1]$. Heavy-mass bands $|3/2, \pm 3/2\rangle$ carry similar information to the light-mass bands $|3/2, \pm 1/2\rangle$. Moreover, $W \rightarrow -W$ for opposite helicity.

limit where SOC exhibits trigonal warping effect, we observe that the circular Rashba contours in the vicinity of Γ point evolves into a rotated boomerang. This happens since the angle-dependent spin splitting dispersion in Eq. (41), takes a $\cos(3\theta)$ form given by

$$\mathcal{G}(\varphi) = \sqrt{\gamma_{1,1}^2 + |\mathbf{k}_\perp|k_z[\gamma_{2,1}^2|\mathbf{k}_\perp|k_z + 2\gamma_{1,1}\gamma_{2,1}\cos(3\varphi)]}. \quad (45)$$

The TAM texture winds twice ($W_n = 2$) around the origin when $E > E_c$ at $|\mathbf{k}| \gtrsim k_c$, see Fig. 4(c). In general, when all SOC terms contribute comparably, the constant-energy contours evolve into a mixed trigonal-hexagonal form, as shown in Fig. 4(d).

Note that for pure modified Rashba SOC contributions, the constant-energy contours are circular because the dispersion depends only on the radial magnitude of the TAM texture. Any dependence on the polar angle φ appears only in the TAM-texture field, not in the energy. However, the polar angle φ becomes important in the spectrum when SOC is mixed.

Importantly, the vorticity phase diagram depends on the out-of-plane momentum k_z . Consequently, the TAM-texture vorticity can change dramatically as k_z increases and states probe deeper into the three-dimensional bulk. As an illustration, Fig. 5 shows the bulk spectrum (constant-energy contours at $k_z \in \{0, \pm 0.5, \pm 1\}$) for a given set of model parameters together with the corresponding vorticity phase diagram. Close to the Γ point at $k_z = 0$, the constant-energy contours are hexagonal, see Fig. 5(a). In this case, the vorticity phase diagram exhibits a conventional Rashba vortex with $W_n = -1$ at small in-plane momentum $|\mathbf{k}_\perp|$ (marked in green) and

an unconventional quintic vortex with $W_n = 5$ at larger $|\mathbf{k}_\perp|$, marked in red. For larger $|k_z|$, the system undergoes a vorticity phase transition where the TAM field acquires a double winding ($W_n = 2$), highlighted in blue in Fig. 5(b). As $|k_z|$ increases further, this $W_n = 2$ region expands while the conventional ($W_n = -1$) regions shrink. Concurrently, the constant-energy contours evolve from hexagonal—with a central circular pocket—to a trigonal shape. By $k_z = \pm 1$, the conventional Rashba-winding region has almost disappeared.

B. TAM-texture for multipolar SOC

When multipolar SOC terms are included in the full Hamiltonian, they induce anisotropy in the heavy-mass band. Consequently, the energy bands can acquire different TAM vorticities. To show this, we assume that the SOC includes the terms $A_{1,-} \otimes A_{1,-} + E_- \otimes E_-$. In this case, the Hamiltonian includes a higher-rank multipolar contribution given by

$$\begin{aligned} \hat{\mathcal{H}}_{\text{soc}}(\mathbf{k}) = & \Upsilon_1(\mathbf{k}) \hat{J}_x + \Lambda_1(\mathbf{k}) \hat{J}_y \\ & + \Upsilon_2(\mathbf{k}) [\hat{J}_x \hat{J}_z^2] + \Lambda_2(\mathbf{k}) [\hat{J}_y \hat{J}_z^2] \\ & + b_1 k_z (3[\hat{J}_y \hat{J}_x^2] - \hat{J}_y^3), \end{aligned} \quad (46)$$

where the first and second lines are the SOC contributions from $\hat{\mathcal{H}}_{\text{MR}}(\mathbf{k})$ and $\hat{\mathcal{H}}_{\text{HS}}^{(1)}(\mathbf{k})$, respectively, and the third line gives the $A_{1,-} \otimes A_{1,-}$ term with strength b_1 .

In this case, the TAM texture no longer obeys the form given in Eq. (37) and becomes anisotropic. Consequently, each energy band exhibits a different TAM texture. In Fig. 6, we present the vorticity phase diagram for $j \in \{1/2, 3/2, 5/2\}$ electrons, obtained from the winding of the TAM texture vector $\mathbf{J}_n(\mathbf{k}) = (\langle \hat{J}_x \rangle_{n\mathbf{k}}, \langle \hat{J}_y \rangle_{n\mathbf{k}})$ where the averages are taken over the Bloch states of Eq. (46).

For $j = 1/2$ electrons, we consider the lowest band, while for $j = 3/2$ and $j = 5/2$ electrons we consider the two and three lowest bands, respectively. The other helical branches have the opposite sign of winding and are not shown. When SOC is purely modified-Rashba form [ignoring the second and third lines in Eq. (46)], the TAM phase diagram is identical for all j degrees of freedom, see Fig. 5(b). Therefore, light-mass electrons with $|m_j| = 1/2$ and heavy-mass electrons with $|m_j| = 3/2, 5/2$ are indistinguishable.

However, the multipolar energy corrections given by the second and third lines in Eq. (46) induce anisotropic TAM textures in both the light- and heavy-mass bands. This is evident by comparing the vorticity phase diagrams for the lowest bands of $j = 1/2$, $j = 3/2$, and $j = 5/2$ electrons, see Fig. 6. For $j = 1/2$ electrons, the quintic vorticity region, marked in red, occupies a large portion of the phase diagram, whereas the twofold-winding region is confined to a small area in the vicinity of the bulk Γ point, see Fig. 6(a). In addition, the linear Rashba regime (marked in green) emerges with increasing k_z , where the TAM texture exhibits a helical form.

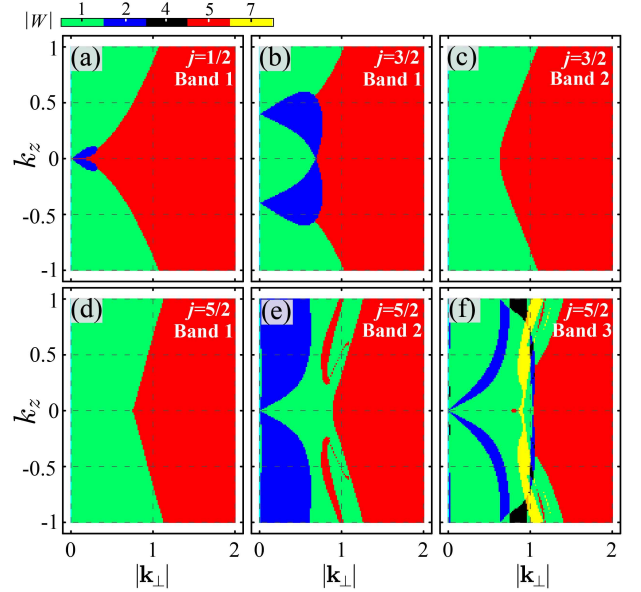


FIG. 6. Total-angular-momentum-vorticity phase diagram for multipolar spin-orbit coupling $A_{1,-} \otimes A_{1,-} + E_- \otimes E_-$ in (a) $j = 1/2$, (b), (c) $j = 3/2$ and (d), (e), (f) $j = 5/2$ basis, shown for one (two) [three] lowest-energy bands, respectively. Remaining bands exhibit identical texture with opposite winding sign. Color bar indicates winding number of $\mathbf{J}_n(\mathbf{k}) = (\langle \hat{J}_x \rangle_{n\mathbf{k}}, \langle \hat{J}_y \rangle_{n\mathbf{k}})$ where $n \in \{1, 2, 3\}$ is band index. Model parameters for multipolar terms are $(\gamma_{1,2}, \gamma_{2,2}, \gamma_{3,2}, \gamma_{4,2})/E_F = (1/2, 1/2, 1/2, 1/2)$ and $b_1 = 0.2 E_F$. Model parameters for modified Rashba term is the same as those in Fig. 5.

Interestingly, in the $j = 3/2$ counterpart shown in Fig. 6(b), the regions of twofold-winding are enhanced and become larger (marked in blue) in band 1. These regions disappear for band 2, shown in Fig. 6(c).

Band 1 for $j = 5/2$ electrons exhibits linear-quintic SOC, see Fig. 6(d). The corresponding phase diagram is almost similar to band 2 of $j = 3/2$ electrons. Interestingly, the anisotropy becomes more pronounced in the second and third lowest bands of $j = 5/2$ electrons. Band 2 evolves into a linear-cubic-quintic admixture. It has the largest area for twofold-winding in the phase diagram, see Fig. 6(e). Importantly, the third lowest energy band, depicted in Fig. 6(f), exhibits exotic phases where the winding number becomes $|W_3^{(j=5/2)}| \in \{4, 7\}$. In this case, the effective SOC energy depends on momenta up to the seventh order.

VI. CURRENT-INDUCED SPIN POLARIZATION

A key manifestation of inversion-symmetry breaking is the Edelstein effect [51], i.e., the generation of a nonequilibrium spin (or more generally TAM) polarization by a dc charge current and, conversely, of a charge current by

a spin imbalance [54, 71]. The Edelstein effect is sensitive to both the underlying texture and the detailed Fermi-surface geometry. It has been explored in Weyl semimetals [69], noncentrosymmetric antiferromagnets [70], superconducting interfaces [87], and two-dimensional materials and Dirac systems [88–90]. In systems where the low-energy states belong to high- j multiplets, it is thus essential to describe Edelstein physics in terms of $\langle \hat{\mathbf{J}} \rangle$ rather than $\langle \hat{\boldsymbol{\sigma}} \rangle$ and to relate the magnitude and anisotropy of the response directly to the structure and winding of the TAM texture on the Fermi surface. In this case, we obtain in the following a counterpart of the Edelstein formalism in TAM representation akin to the spin-1/2 basis [51, 53, 72].

Considering an electric field along the x -axis, i.e., $\mathbf{E} = (E_x, 0)$, it induces a positive spin accumulation perpendicular to the field direction, specifically along the y -axis. A linear response to the field, under the Boltzmann approximation, leads to a net finite TAM average $\langle J_\alpha^{(j)} \rangle$ with $j \in \{1/2, 3/2, 5/2\}$, given by $\langle J_\alpha^{(j)} \rangle = \sum_\beta \chi_{\alpha\beta}^{(j)} E_\beta$ where $\chi_{\alpha\beta}^{(j)}$ denotes the 3×2 Edelstein susceptibility tensor for angular momentum j , $\alpha \in \{x, y, z\}$, and $\beta \in \{x, y\}$. Here, the components of the tensor are given by [53, 69, 72, 91]

$$\chi_{\alpha\beta}^{(j)} = e\tau \sum_{n=1}^{2j+1} \int \frac{d^2 \mathbf{k}_\perp}{(2\pi)^2} J_n^{(\alpha)}(\mathbf{k}_\perp) v_n^{(\beta)}(\mathbf{k}_\perp) \mathcal{F}_{n,\mathbf{k}_\perp}, \quad (47)$$

where $\mathbf{k}_\perp = (k_x, k_y, 0)$ is the in-plane momentum, and the function $\mathcal{F}_{n,\mathbf{k}_\perp} = -\partial f_0 / \partial E$ denotes the thermal broadening kernel of the linear response, k_B is the Boltzmann constant, T is temperature, e and τ denote carrier charge and momentum relaxation time, respectively. The TAM texture component is $\mathbf{J}_n^{(\alpha)}(\mathbf{k}_\perp) = \langle n, \mathbf{k}_\perp | \hat{J}_\alpha | n, \mathbf{k}_\perp \rangle$, and $v_n^{(\beta)}(\mathbf{k}_\perp) = \langle n, \mathbf{k}_\perp | \partial \hat{H} / \partial k_\beta | n, \mathbf{k}_\perp \rangle$ denotes the group velocity for the n -th energy band with the eigenbasis $|n, \mathbf{k}_\perp\rangle$.

Up to linear order in the momentum-dependent SOC and for an isotropic Fermi surface, the components of the Edelstein tensor satisfy $\chi_{xy} = -\chi_{yx}$ and $\chi_{xx} = \chi_{yy} = 0$. The vanishing of the diagonal components follows from the angular integration in polar coordinates, $\chi_{xx} \propto \int_0^{2\pi} \sin \theta \cos \theta d\theta = 0$. At zero temperature, the Edelstein susceptibility $\chi_{\alpha\beta}^{(j)}/e\tau$ is determined solely by the Fermi contours (FCs), since $\mathcal{F} = \delta(E_\nu - \mu_c)$ where $\mu_c = E_F$. Consequently, one can write [53]

$$\chi_{xy}^{(j)}/c_0 = \sum_n \oint_{\text{FC}_n} ds_{\text{FC}_n} J_n^{(x)}(\mathbf{k}_\perp) \hat{v}_n^{(y)}(\mathbf{k}_\perp), \quad (48)$$

where $c_0 \equiv e\tau/(2\pi)^2$, $\hat{v}_n^{(y)} = v_n^{(y)} / |\mathbf{v}_n|$ is the y -component of the unit velocity vector, taking values $\hat{v}_n^{(y)} \in [-1, 1]$, $\mathbf{v}_n = (v_n^{(x)}, v_n^{(y)})$ is the 2D group-velocity vector, and ds_{FC_n} is the arc length element along the n -th Fermi contour. For a circular Fermi surface, we have $ds_{\text{FC}_n} = |\mathbf{k}_F^n| d\theta$. Thus, the Edelstein susceptibility measures the

net TAM polarization along the y -direction carried by states at the Fermi level. The corresponding imbalance of TAM-polarized carriers can couple to the electric field and is transported along the group-velocity direction [69, 87].

In Fig. 7, we show the dependence of TAM accumulation in the y -direction on the chemical potential for different angular momenta $j \in \{1/2, 3/2, 5/2\}$. Notably, the Edelstein effect is enhanced and exhibits a broader plateau when the TAM degrees of freedom are enlarged and the states are mostly occupied, as seen by comparing the blue and black lines in Fig. 7.

There is no Edelstein effect for $j = 1/2$ states in the energy window $\mu_c/E_F \in [0, 0.7]$, see red line in Fig. 7(a). In this regime, the Fermi level lies below the onset of the Rashba-split bands so that no Fermi contour contributes to the response. As the chemical potential increases, the electric field modifies the occupation of states near the Fermi level and a TAM accumulation forms along the y -direction. For $\mu_c/E_F \gtrsim 0.7$, only the lower branch E_{-, \mathbf{k}_\perp} , which is partially occupied, intersects the Fermi level and contributes to $\chi_{xy}^{(1/2)}$. In this case, the two Fermi momenta (which we denote by $|\mathbf{k}_F^\pm|$ for the inner and outer radii) originate from a *single* energy band whose minimum occurs at finite $|\mathbf{k}_\perp|$, i.e., a Mexican-hat-like dispersion. Consequently, $\chi_{xy}^{(1/2)}$ depends strongly on the chemical potential and grows with μ_c until the upper branch E_{+, \mathbf{k}_\perp} also becomes occupied.

Once both helical branches are present at the Fermi level, the difference between the spin-split Fermi radii becomes independent of μ_c , and the Edelstein response saturates at a plateau. This is because the Rashba spin splitting is isotropic in momentum space [92]. This can be analytically deduced from the spin-1/2 model Hamiltonian that includes both the kinetic and Rashba SOC, i.e.,

$$H_0 = \mathcal{A}_1 + \gamma_{1,1} (k_x \hat{J}_y - k_y \hat{J}_x), \quad (49)$$

where $\mathcal{A}_1 = \mu_1 + a_{1,1} |\mathbf{k}_\perp|^2$ and $\hat{J}_i \rightarrow \hat{\sigma}_i$ is the Pauli matrices. The spectrum for H_0 is $E_{n, \mathbf{k}_\perp} = \mathcal{A}_1 + n\gamma_{1,1} |\mathbf{k}_\perp|$ where $|\mathbf{k}_\perp| = \sqrt{k_x^2 + k_y^2}$ and $n = \pm$. The relevant group velocity vector is $\mathbf{v}_n = (v_n^{(x)}, v_n^{(y)})$ and $v_n^{(i)} = 2a_{1,1} k_i + n\gamma_{1,1} k_i / |\mathbf{k}_\perp|$ with $i \in \{x, y\}$. In addition, the TAM texture vector for H_0 becomes $\mathbf{J}_\pm = \pm(1/|\mathbf{k}_\perp|)(-k_y, k_x)$ that is perpendicular to the momentum direction, i.e., $\mathbf{J}_\pm \cdot \mathbf{k}_\perp = 0$. The Fermi contours are circular $|\mathbf{k}_F^\pm|^2 \equiv k_x^2 + k_y^2$ with radius

$$|\mathbf{k}_{n,F}^{(l)}| = \frac{1}{2a_{1,1}} \left(-n\gamma_{1,1} + (-1)^l \sqrt{1 + 4a_{1,1}(\mu_c - \mu_1)} \right), \quad (50)$$

where $l \in \{1, 2\}$ denoting two root solutions per given band. Considering polar coordinate and after some algebra, we obtain the Edelstein susceptibility

$$\chi_{xy}^{(1/2)}/\pi = - \sum_n n \operatorname{sgn}(2a_{1,1} |\mathbf{k}_F^n| + n\gamma_{1,1}) |\mathbf{k}_F^n|, \quad (51)$$

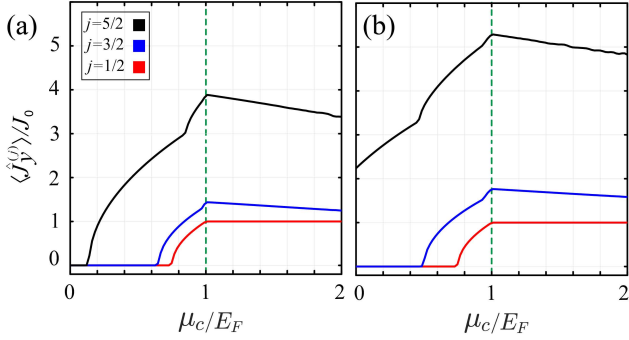


FIG. 7. Edelstein effect for total angular momenta $j \in \{1/2, 3/2, 5/2\}$ in a non-centrosymmetric spin-orbit coupled model Hamiltonian in Eq. (3) that preserves time-reversal and C_{3v} point group. Perpendicular total-angular-momentum expectation value $\langle \hat{J}_y^{(j)} \rangle$ induced by an external electric field $\mathbf{E} = (1, 0)$ for (a) a pure modified Rashba SOC $(\tilde{\gamma}_1, \tilde{\gamma}_2) = (-1, 0)$ and (b) an admixture of both SOC terms with $(\tilde{\gamma}_1, \tilde{\gamma}_2) = (-1, -0.3)$, where $\tilde{\gamma}_i \equiv \gamma_{1,i}/E_F$. Model parameters for even-parity sector $\hat{\mathcal{H}}_t$ are $(\tilde{\alpha}_1, \tilde{\alpha}_2, \tilde{\mu}_2, \tilde{\alpha}'_1, \tilde{\alpha}'_2) = (1, 0, 0, 1, 0)$ where $\tilde{\alpha}_i \equiv \alpha_{1,i}/E_F$ and $\tilde{\alpha}'_i \equiv \alpha_{2,i}/E_F$. Other parameters are $J_0 = N_0 \max(|\langle \hat{J}_y^{(1/2)} \rangle|)$, $\chi_0 = N_0 \max(|\langle \chi_{xy}^{(1/2)} \rangle|)$ where $N_0 = e\tau/(2\pi)^2$ and $E_F = \mu_1$. In the numerics, we replace the Dirac delta function with a Gaussian function $\delta(E_{n,\mathbf{k}_\perp} - \mu_c) \equiv (1/\Omega\sqrt{2\pi}) \exp[-(E_{n,\mathbf{k}_\perp} - \mu_c)^2/\Omega^2]$ with broadening factor $\Omega \approx 7.4 \times 10^{-3}$.

where it results in

$$\chi_{xy}^{(1/2)}/c_0\pi = |\mathbf{k}_F^-| - |\mathbf{k}_F^+| = \frac{\gamma_{1,1}}{a_{1,1}}, \quad (52)$$

where $\chi_{xy}^{(1/2)}$ is independent of μ_c for $\mu_c > \mu_1$, see the red plateau in Fig. 7(a). At $\gamma_{1,1} = 0$, the response is vanishing $\chi_{xy}^{(1/2)} = 0$ because $|\mathbf{k}_F^-| = |\mathbf{k}_F^+|$.

Importantly, in $j > 1/2$ systems this saturation is no longer perfectly flat: $\chi_{xy}^{(j)}$ continues to vary smoothly with the chemical potential, as seen from the black and blue lines in Fig. 7(a). This is because higher TAM introduces additional m_j -dependent subbands and increases the number of Fermi contours, leading to a more complex evolution of the Fermi surface as μ_c is tuned.

Importantly, when the multipolar SOC terms are included in the Hamiltonian, the Edelstein effect can be further enhanced for the $j = 3/2$ and $j = 5/2$ electrons, see Fig. 7(b). To see this, consider the multipolar SOC Hamiltonian

$$H = H_0 + \mathcal{A}_2 \hat{J}_z^2 + \gamma_{1,2} (k_x \lceil \hat{J}_y \hat{J}_z^2 \rceil - k_y \lceil \hat{J}_x \hat{J}_z^2 \rceil), \quad (53)$$

where the second term represents m_j -dependent energy shifts, and the third term is the multipolar Rashba effect for $j \in \{3/2, 5/2\}$. This modification changes the density of states near the Fermi level. Additionally, the number of Fermi contours can increase to four (six) through energy shifts $\mathcal{A}_2 \hat{J}_z^2$, resulting in larger values, i.e., $\langle J_y^{(5/2)} \rangle > \langle J_y^{(3/2)} \rangle > \langle J_y^{(1/2)} \rangle$. In the limit $\gamma_{1,2} = 0$,

the enhancement of the Edelstein effect originates from the energy shifts for electrons with different m_j , induced by the multipolar term \hat{J}_z^2 .

Note that the Edelstein effect is absent in $\hat{\mathcal{H}}_{HS}^{(2)}$, since the SOC contribution from the multipolar doublet generator $(1/2) \llbracket (\hat{J}_y^2 - \hat{J}_x^2) \hat{J}_z \rrbracket, \llbracket \hat{J}_x \hat{J}_y \hat{J}_z \rrbracket$ is purely of interband character, with a vanishing in-plane TAM texture. Although this doublet exhibits an out-of-plane TAM texture, an in-plane electric field E_x cannot generate an Edelstein response in the z -direction because of the mirror symmetry in the xz -plane. The linear response must be invariant under this mirror reflection so that $\langle J_z^{(j)} \rangle = \langle J_z^{(j)} \rangle$, while the axial nature of TAM implies $\langle J_z^{(j)} \rangle = -\langle J_z^{(j)} \rangle$. These two conditions are only compatible if $\chi_{xz} = 0$.

VII. CONCLUSION

In this work, we develop a theoretical framework to quantify spin-orbit coupling in p - and d -electrons of heavy elements. We focus on Bloch states constrained by time-reversal and C_{3v} point-group symmetry, as realized, for example, in PtBi₂ and BiTeI [55–57, 59]. Within this setting, the total angular momentum is conserved and the bands decompose into well-defined j -multiplets such as $j = 3/2$ and $j = 5/2$. Our multipolar SOC framework is particularly relevant when a conventional Rashba description cannot fully capture the observed band splittings, as realized in BiTeI [60].

We show that in strongly spin-orbit-coupled systems the TAM vector forms a texture in reciprocal space, as an analogue of the conventional spin-1/2 texture. When multipolar corrections dominate the dipolar SOC energy, the TAM texture becomes anisotropic per energy bands. In particular, the TAM texture of heavy-mass electrons differs from that of light-mass electrons, in contrast to the dipolar Rashba model. They exhibit different varieties of winding at small and large momenta in the vicinity of the 3D Γ point. In addition, we quantify the substantial enhancement of spin-orbit splitting for electrons with $j > 1/2$. We further demonstrated that these multipolar energy corrections can enhance spintronic responses, such as current-induced polarization.

It is worth mentioning that resolving TAM multiplets experimentally is challenging. X-ray magnetic circular dichroism is a powerful probe of SOC in j -shell electrons, providing information on spin and orbital moments through polarization-dependent absorption [93, 94]. Resonant inelastic x-ray scattering at appropriate absorption edges is complementary, giving bulk-sensitive access to intra-multiplet and spin-orbit excitations characteristic of j -manifolds in correlated 4d/5d or 4f/5f systems [95, 96]. We additionally propose the development of j -resolved scanning probes with quadrupolar or more general multipolar magnetic configurations, for example based on d -wave altermagnets [97], tunable ferromagnetic

alloys [98], or multipolar complex oxides [99]. In addition, the orbital component of $\langle \mathbf{J} \rangle$ in $j > 1/2$ electrons is dominant, highlighting an intrinsically orbital-driven character of the TAM response and supporting orbitronic applications [100–106].

VIII. ACKNOWLEDGMENTS

We thank Chang-An Li for fruitful discussions. This work was supported by the Deutsche Forschungsgemeinschaft (DFG, German Research Foundation) through SFB 1170 (project ID 258499086), SFB 1143 (project ID 247310070, project A04), and the Würzburg-Dresden Cluster of Excellence ctd.qmat (EXC 2147, project ID 390858490).

Appendix A: Decomposition of j into C_{3v} irreducible representations

We assume that SOC is strong compared to the kinetic energy. In this case, the TAM is conserved with values $J \in [|l - S|, |l + S|]$. The splitting of an energy level, labeled with integer J , is the same as for l . However, half-integer J is not and it should be treated using a double-group representation. In this case, the double group character table for the C_{3v} point group is given in Table III. The number of irreps in this table is twice that of the ordinary (single) character table. This doubling arises because a fermionic state does not return to itself under a $\theta \rightarrow \theta + 2\pi$ rotation; instead, it requires a $\theta \rightarrow \theta + 4\pi$ rotation to remain invariant. In this context, the spin characters under a 2π rotation transform as

$$X^J(R_{\theta+2\pi}) = (-1)^{2J} X^J(R_\theta), \quad (\text{A1})$$

where $R_\theta \in \{E, 2C_{3z}, 3\sigma_v\}$ and

$$X^J(R_\theta) = \frac{\sin((J+1/2)\theta)}{\sin(\theta/2)}. \quad (\text{A2})$$

To determine how the representation D_J decomposes into the irreps Γ_i , we use the decomposition formula $D_J = \sum_{i=1}^6 a_i \Gamma_i$ where the coefficients are given by

$$a_i = \frac{1}{h} \sum N_{R_\theta} D_J^*(R_\theta) \Gamma_i(R_\theta), \quad (\text{A3})$$

with N_{R_θ} denoting the number of occurrences of the symmetry operation R_θ and $h = 12$ being the order of the double group. After plugging the results of Tables III and IV into Eq. (A3), we obtain the decomposition of quantum states under strong SOC

$$D_{1/2} \rightarrow \Gamma_4, \quad (\text{A4})$$

$$D_{3/2} \rightarrow \Gamma_4 + \Gamma_5 + \Gamma_6, \quad (\text{A5})$$

$$D_{5/2} \rightarrow 2\Gamma_4 + \Gamma_5 + \Gamma_6, \quad (\text{A6})$$

Table III. Double-group character table of the point group C_{3v} for treating half-integer quantum numbers at high symmetry points Γ, A, H, K .

	E	\bar{E}	$2C_{3z}$	$2\bar{C}_{3z}$	$3\sigma_v$	$3\bar{\sigma}_v$
Γ_1	1	1	1	1	1	1
Γ_2	1	1	1	1	-1	-1
Γ_3	2	2	-1	-1	0	0
Γ_4	2	-2	1	-1	0	0
Γ_5	1	-1	-1	1	i	$-i$
Γ_6	1	-1	-1	1	$-i$	i

Table IV. Double-group character table for half-integer total angular momentum $J \in \{1/2, 3/2, 5/2\}$.

	E	\bar{E}	$2C_{3z}$	$2\bar{C}_{3z}$	$3\sigma_v$	$3\bar{\sigma}_v$
$D_{1/2}$	2	-2	1	-1	0	0
$D_{3/2}$	4	-4	-1	1	0	0
$D_{5/2}$	6	-6	0	0	0	0

where the $D_{1/2}$ states remain doubly degenerate labeled with Γ_4 in the presence of a crystal field, while $D_{3/2}$ and $D_{5/2}$ states split into one (two) doubly degenerate representations and two one-dimensional states corresponding to complex conjugate irreps Γ_5 and Γ_6 . These two irreps form a reducible 2D representation as $\Gamma_{3/2} \equiv \Gamma_5 \oplus \Gamma_6$. Note that $D_{3/2}$ ($D_{5/2}$) is a four-dimensional (six-dimensional) representation of the full rotational group comprising of four (six) magnetic sub-levels labeled by $m_j \in \{\pm 1/2, \pm 3/2\}$ ($m_j \in \{\pm 1/2, \pm 3/2, \pm 5/2\}$). Importantly, the dimension of Γ_5 and Γ_6 are restricted to 1 because of the dimensionality $\sum_{i=1}^6 l_i^2 = h$ where l_i is the dimension of irreps given in the second column of Table III. Consequently, we have $1^2 + 1^2 + 2^2 + 2^2 + l_5^2 + l_6^2 = 12$, resulting in $l_5^2 + l_6^2 = 2$, where $l_5 = l_6 = 1$ is the only possible solution.

Appendix B: Point-Group and Time-Reversal Constraints in the $j > 1/2$ basis

In this Appendix, we present a detailed construction of the $\mathbf{k} \cdot \mathbf{p}$ model that preserves both the C_{3v} point-group symmetry and time-reversal symmetry T . Using group-theoretical methods, we identify all momentum-dependent basis polynomials and TAM-tensor matrices that transform under the gray magnetic point group $\mathcal{M}_{3v} = C_{3v} + TC_{3v}$. The relevant character table is given in Table V. The characters of magnetic irreps that are odd under time-reversal are obtained by flipping the sign of the characters of the corresponding time-reversal-even representations. By taking direct products of these momenta and TAM representations, we obtain the multipolar SOC terms near the Γ point of the three-dimensional bulk Brillouin zone.

Table V. Character table of \mathcal{M}_{3v} gray magnetic point group. irreps are labeled by their behavior under time-reversal symmetry, with the last column indicating whether each representation is even or odd under the action of T .

	E	$2C_{3z}$	$3\sigma_v$	$2TC_{3z}$	$3T\sigma_v$	T
$A_{1,+}$	+1	+1	+1	+1	+1	+1
$A_{2,+}$	+1	+1	-1	+1	-1	+1
E_+	+2	-1	0	-1	0	+2
$A_{1,-}$	+1	+1	+1	-1	-1	-1
$A_{2,-}$	+1	+1	-1	-1	+1	-1
E_-	+2	-1	0	+1	0	-2

We focus on TAM values $j \in \{3/2, 5/2\}$. This choice is motivated by the strong interaction between the electron spin and the d -orbital degrees of freedom. Our goal is to construct the analogue of the Pauli spin vector in a $j > 1/2$ basis, i.e.,

$$\hat{\mathbf{J}} = (\hat{J}_x, \hat{J}_y, \hat{J}_z), \quad (\text{B1})$$

with $[\hat{J}_i, \hat{J}_j] = i\epsilon_{ijk}\hat{J}_k$. The eigenstates $|j, m_j\rangle$ satisfy

$$\hat{J}_z|j, m_j\rangle = m_j|j, m_j\rangle \quad (\text{B2})$$

so that \hat{J}_z is diagonal in this basis,

$$\hat{J}_z = \frac{1}{2} \text{diag}(5, 3, 1, -1, -3, -5). \quad (\text{B3})$$

To obtain the x - and y -components of the vector operator $\hat{\mathbf{J}}$, we introduce the ladder operators

$$\hat{J}_\pm = \hat{J}_x \pm i\hat{J}_y, \quad (\text{B4})$$

which act on the basis states as

$$J_\pm|j, m_j\rangle = \sqrt{j(j+1) - m_j(m_j \pm 1)}|j, m_j \pm 1\rangle, \quad (\text{B5})$$

where $[J_z, J_\pm] = \pm J_\pm$. Using Eq. (B5), we obtain matrix form for $\hat{J}_{x(y)}$, for instance in $j = 5/2$ basis, as given by

$$\hat{J}_x = \begin{pmatrix} 0 & \frac{\sqrt{5}}{2} & 0 & 0 & 0 & 0 \\ \frac{\sqrt{5}}{2} & 0 & \sqrt{2} & 0 & 0 & 0 \\ 0 & \sqrt{2} & 0 & \frac{3}{2} & 0 & 0 \\ 0 & 0 & \frac{3}{2} & 0 & \sqrt{2} & 0 \\ 0 & 0 & 0 & \sqrt{2} & 0 & \frac{\sqrt{5}}{2} \\ 0 & 0 & 0 & 0 & \frac{\sqrt{5}}{2} & 0 \end{pmatrix}, \quad (\text{B6})$$

$$\hat{J}_y = \begin{pmatrix} 0 & \frac{i\sqrt{5}}{2} & 0 & 0 & 0 & 0 \\ \frac{-i\sqrt{5}}{2} & 0 & i\sqrt{2} & 0 & 0 & 0 \\ 0 & -i\sqrt{2} & 0 & \frac{3i}{2} & 0 & 0 \\ 0 & 0 & \frac{-3i}{2} & 0 & i\sqrt{2} & 0 \\ 0 & 0 & 0 & -i\sqrt{2} & 0 & \frac{i\sqrt{5}}{2} \\ 0 & 0 & 0 & 0 & \frac{-i\sqrt{5}}{2} & 0 \end{pmatrix}. \quad (\text{B7})$$

To analyze the symmetry operations of the magnetic point group \mathcal{M}_{3v} , we express its elements as matrices in the $j > 1/2$ basis. The nonmagnetic subgroup C_{3v} consists of

$$g \in \{E, C_{3z}, C_{3z}^2, \sigma_{v_1}, \sigma_{v_2}, \sigma_{v_3}\}, \quad (\text{B8})$$

where E is the identity operation and C_{3z} (C_{3z}^2) denotes a threefold rotation around the z -axis by an angle $\theta = 2\pi/3$ ($4\pi/3$). The matrix representation of C_{3z} is given by

$$\hat{C}_{3z} \equiv e^{-2\pi i \hat{J}_z/3} = \begin{pmatrix} \nu & 0 & 0 & 0 & 0 & 0 \\ 0 & -1 & 0 & 0 & 0 & 0 \\ 0 & 0 & \nu^* & 0 & 0 & 0 \\ 0 & 0 & 0 & \nu & 0 & 0 \\ 0 & 0 & 0 & 0 & -1 & 0 \\ 0 & 0 & 0 & 0 & 0 & \nu^* \end{pmatrix}, \quad (\text{B9})$$

where $\nu = e^{i\pi/3}$. In Eq. (B8), the mirror reflection σ_{v_1} is implemented in the TAM basis as a π -rotation about the y -axis, i.e.,

$$\hat{\sigma}_{v_1} \equiv e^{-i\pi \hat{J}_y} = \begin{pmatrix} 0 & 0 & 0 & 0 & 0 & 1 \\ 0 & 0 & 0 & 0 & -1 & 0 \\ 0 & 0 & 0 & 1 & 0 & 0 \\ 0 & 0 & -1 & 0 & 0 & 0 \\ 0 & 1 & 0 & 0 & 0 & 0 \\ -1 & 0 & 0 & 0 & 0 & 0 \end{pmatrix}. \quad (\text{B10})$$

This implies that under the σ_{v_1} operation, the wave vector and the TAM vector transform differently.

$$\sigma_{v_1} : \begin{cases} \mathbf{k} \rightarrow (+k_x, -k_y, +k_z), \\ \hat{\mathbf{J}} \rightarrow (-\hat{J}_x, \hat{J}_y, -\hat{J}_z). \end{cases} \quad (\text{B11})$$

The other two mirror operators, $\hat{\sigma}_{v_2}$ and $\hat{\sigma}_{v_3}$, can be obtained by rotating $\hat{\sigma}_{v_1}$ around the z -axis by an angle of $\theta = 2\pi/3$ and $\theta = 4\pi/3$, respectively given by

$$\hat{\sigma}_{v_2} = \hat{C}_{3z} \hat{\sigma}_{v_1} [\hat{C}_{3z}]^\dagger = \begin{pmatrix} 0 & 0 & 0 & 0 & 0 & \nu' \\ 0 & 0 & 0 & 0 & -1 & 0 \\ 0 & 0 & 0 & \nu'^* & 0 & 0 \\ 0 & 0 & -\nu' & 0 & 0 & 0 \\ 0 & 1 & 0 & 0 & 0 & 0 \\ -\nu'^* & 0 & 0 & 0 & 0 & 0 \end{pmatrix}, \quad (\text{B12})$$

$$\hat{\sigma}_{v_3} = \hat{C}_{3z}^2 \hat{\sigma}_{v_1} [\hat{C}_{3z}^2]^\dagger = \hat{\sigma}_{v_2}^*, \quad (\text{B13})$$

where $\nu' = e^{2i\pi/3}$. To proceed further, it is important to understand how the TAM vector $\hat{\mathbf{J}}$ and the wave vector \mathbf{k} transform under the magnetic point group \mathcal{M}_{3v} . In general, both vectors transform according to the symmetry operations of \mathcal{M}_{3v} such that

$$\hat{g}\hat{\mathbf{J}}\hat{g}^\dagger \mapsto \hat{\mathbf{J}}', \quad (\text{B14})$$

$$\hat{R}^{-1}\mathbf{k} \mapsto \mathbf{k}'. \quad (\text{B15})$$

Table VI. Wave vector $\mathbf{k} = (k_x, k_y, k_z)$ and total-angular-momentum vector $\hat{\mathbf{J}} = (\hat{J}_x, \hat{J}_y, \hat{J}_z)$ under \mathcal{M}_{3v} magnetic point group symmetry.

	\mathbf{k}			$\hat{\mathbf{J}}$		
E	k_x	k_y	k_z	\hat{J}_x	\hat{J}_y	\hat{J}_z
C_{3z}	$\frac{-1}{2}k_x - \frac{\sqrt{3}}{2}k_y$	$\frac{\sqrt{3}}{2}k_x - \frac{1}{2}k_y$	k_z	$\frac{-1}{2}\hat{J}_x + \frac{\sqrt{3}}{2}\hat{J}_y$	$\frac{-\sqrt{3}}{2}\hat{J}_x - \frac{1}{2}\hat{J}_y$	\hat{J}_z
C_{3z}^2	$\frac{-1}{2}k_x + \frac{\sqrt{3}}{2}k_y$	$\frac{-\sqrt{3}}{2}k_x - \frac{1}{2}k_y$	k_z	$\frac{-1}{2}\hat{J}_x - \frac{\sqrt{3}}{2}\hat{J}_y$	$\frac{\sqrt{3}}{2}\hat{J}_x - \frac{1}{2}\hat{J}_y$	\hat{J}_z
σ_{v_1}	k_x	$-k_y$	k_z	$-\hat{J}_x$	\hat{J}_y	$-\hat{J}_z$
σ_{v_2}	$\frac{-1}{2}k_x + \frac{\sqrt{3}}{2}k_y$	$\frac{\sqrt{3}}{2}k_x + \frac{1}{2}k_y$	k_z	$\frac{1}{2}\hat{J}_x - \frac{\sqrt{3}}{2}\hat{J}_y$	$\frac{-\sqrt{3}}{2}\hat{J}_x - \frac{1}{2}\hat{J}_y$	$-\hat{J}_z$
σ_{v_3}	$\frac{-1}{2}k_x - \frac{\sqrt{3}}{2}k_y$	$\frac{-\sqrt{3}}{2}k_x + \frac{1}{2}k_y$	k_z	$\frac{1}{2}\hat{J}_x + \frac{\sqrt{3}}{2}\hat{J}_y$	$\frac{\sqrt{3}}{2}\hat{J}_x - \frac{1}{2}\hat{J}_y$	$-\hat{J}_z$
TC_{3z}	$\frac{1}{2}k_x + \frac{\sqrt{3}}{2}k_y$	$\frac{1}{2}k_y - \frac{\sqrt{3}}{2}k_x$	$-k_z$	$\frac{1}{2}\hat{J}_x - \frac{\sqrt{3}}{2}\hat{J}_y$	$\frac{\sqrt{3}}{2}\hat{J}_x + \frac{1}{2}\hat{J}_y$	$-\hat{J}_z$
TC_{3z}^2	$\frac{1}{2}k_x - \frac{\sqrt{3}}{2}k_y$	$\frac{\sqrt{3}}{2}k_x + \frac{1}{2}k_y$	$-k_z$	$\frac{1}{2}\hat{J}_x + \frac{\sqrt{3}}{2}\hat{J}_y$	$\frac{-\sqrt{3}}{2}\hat{J}_x + \frac{1}{2}\hat{J}_y$	$-\hat{J}_z$
$T\sigma_{v_1}$	$-k_x$	k_y	$-k_z$	\hat{J}_x	$-\hat{J}_y$	\hat{J}_z
$T\sigma_{v_2}$	$\frac{1}{2}k_x - \frac{\sqrt{3}}{2}k_y$	$\frac{-\sqrt{3}}{2}k_x - \frac{1}{2}k_y$	$-k_z$	$\frac{-1}{2}\hat{J}_x + \frac{\sqrt{3}}{2}\hat{J}_y$	$\frac{\sqrt{3}}{2}\hat{J}_x + \frac{1}{2}\hat{J}_y$	\hat{J}_z
$T\sigma_{v_3}$	$\frac{1}{2}k_x + \frac{\sqrt{3}}{2}k_y$	$\frac{\sqrt{3}}{2}k_x - \frac{1}{2}k_y$	$-k_z$	$\frac{-1}{2}\hat{J}_x - \frac{\sqrt{3}}{2}\hat{J}_y$	$\frac{-\sqrt{3}}{2}\hat{J}_x + \frac{1}{2}\hat{J}_y$	\hat{J}_z
T	$-k_x$	$-k_y$	$-k_z$	$-\hat{J}_x$	$-\hat{J}_y$	$-\hat{J}_z$

Table VII. Character of $E_- \otimes E_-$ product.

	E	C_{3z}	σ_v	TE	TC_{3z}	$T\sigma_v$
E_-	2	-1	0	-2	1	0
$E_- \otimes E_-$	4	1	0	4	1	0

The transformation properties of $\hat{\mathbf{J}}'$ and \mathbf{k}' under all symmetry operations are summarized in Table VI.

Importantly, \hat{J}_0 and \hat{J}_z transform according to the irreps $A_{1,+}$ and $A_{2,-}$, respectively, while (\hat{J}_x, \hat{J}_y) form a doublet transforming under the E_- irrep. The subscript of irreps, namely E_- (E_+), denotes the character of the time-reversal operator, which can be odd (even). In addition, the momentum components (k_x, k_y) transform as the E_- irrep and k_z transforms according to the $A_{1,-}$ irrep. These transformation properties provide a key starting point for constructing higher-order momentum-dependent polynomial terms that are compatible with the symmetry of the magnetic group \mathcal{M}_{3v} . The resulting polynomials, up to fifth order, are summarized in Table X, and are derived by applying direct products of irreps as detailed in Table IX. For instance, a second-order polynomial that transforms according to the E_+ irrep can be constructed by taking the direct product of two basis functions transforming as E_- . This relation is expressed as $E_+ = E_- \otimes E_-$, which which the relevant characters are listed in Table VII, where the first row lists the symmetry elements of the \mathcal{M}_{3v} group, while the second and third rows show the character values for the irrep E_- , and its direct product $E_- \otimes E_-$. We infer that this direct product is a reducible representation, as its dimensionality exceeds that of a typical two-dimensional irrep. Specifically, the character of the identity element E in Table VII is four, indicating a four-dimensional representation. Therefore, this reducible representation de-

Table VIII. Character for direct sum of irreps from decomposition $E_+ \otimes E_+$.

	E	C_{3z}	σ_v	TE	TC_{3z}	$T\sigma_v$
$A_{1,+}$	1	1	1	1	1	1
$A_{2,+}$	1	1	-1	1	1	-1
E_+	2	-1	0	2	-1	0
$A_{1,+} \oplus A_{2,+} \oplus E_+$	4	1	0	4	1	0

composes into a direct sum of irreps as

$$E_- \otimes E_- \rightarrow A_{1,+} \oplus A_{2,+} \oplus E_+. \quad (B16)$$

This decomposition is confirmed by summing the characters of the corresponding irreps, as listed in Table VIII. In accordance, the reducible representation $E_+ = E_- \otimes E_-$ contains four momentum-dependent components, expressed as

$$(k_x, k_y) \otimes (k_x, k_y) = (k_x^2, k_y^2, k_x k_y, k_y k_x). \quad (B17)$$

Note that only certain linear combinations of these components transform according to the E_+ irrep. In particular, the pair $(k_x^2 - k_y^2, k_x k_y)$ transforms as the E_+ irrep, while the scalar $k_x^2 + k_y^2$ transforms according to $A_{1,+}$. However, it is not possible to form a second-order polynomial from these terms that transforms as $A_{2,+}$. Therefore, the $A_{2,+}$ representation does not appear at second order in momentum, see Table X.

Appendix C: Multipolar SOC Construction in \mathcal{M}_{3v} Symmetry

To construct a 3D bulk model Hamiltonian, we utilize the momentum-dependent polynomials listed in Table X and combine them with the appropriate TAM tensor matrices transforming according to the $A_{1,+}$ irrep. Since the

Table IX. Direct product of irreducible representations in \mathcal{M}_{3v} gray magnetic group. Subscript follows product rules $1 \otimes 2 = 2$, $1 \otimes 1 = 1$, $2 \otimes 2 = 1$, $\pm \otimes \pm = +$, and $-\otimes+ = -$. $A_{1,+}$ is shown in bold, indicating symmetry-allowed SOC terms from the corresponding direct product. We have defined $Q_- \equiv A_{1,-} \oplus A_{2,-} \oplus E_-$ and $\mathbf{Q}_+ \equiv \mathbf{A}_{1,+} \oplus A_{2,+} \oplus E_+$.

$A_{1,+}$	$A_{2,+}$	E_+	$A_{1,-}$	$A_{2,-}$	E_-
$A_{1,+}$	$A_{1,+}$	$A_{2,+}$	E_+	$A_{1,-}$	$A_{2,-}$
$A_{2,+}$	$A_{2,+}$	$A_{1,+}$	E_+	$A_{2,-}$	E_-
E_+	E_+	E_+	Q_+	E_-	E_-
$A_{1,-}$	$A_{1,-}$	$A_{2,-}$	E_-	$A_{1,+}$	$A_{2,+}$
$A_{2,-}$	$A_{2,-}$	$A_{1,-}$	E_-	$A_{2,+}$	$A_{1,+}$
E_-	E_-	E_-	Q_-	E_+	E_+
					Q_+

Table X. Momentum-dependent polynomials transforming according to \mathcal{M}_{3v} magnetic point group. Order of each polynomial corresponds to order of associated spherical harmonics. A cross symbol (\times) indicates that no polynomial basis exists for given irreducible representation.

$A_{1,+}$	1	k_z^2	$k_z^4, k_z(k_x^3 - 3k_x k_y^2)$
$A_{2,+}$	\times	\times	$k_z(3k_y k_x^2 - k_y^3)$
E_+	\times	$\binom{k_x^2 - k_y^2}{k_x k_y}$	$\binom{[k_x^2 - k_y^2]k_z^2}{k_x k_y k_z^2}$
	\times	$\binom{k_x k_z}{k_y k_z}$	$\binom{k_x k_z^3}{k_y k_z^3}$
	\times	\times	$\binom{[k_x^2 - k_y^2]^2 - 4k_x^2 k_y^2}{k_x k_y [k_x^2 - k_y^2]}$
$A_{1,-}$	k_z	$k_x^3 - 3k_x k_y^2, k_z^3$	$k_z^2(k_x^3 - 3k_x k_y^2), k_z^5$
$A_{2,-}$	\times	$3k_y k_x^2 - k_y^3$	$(3k_y k_x^2 - k_y^3)k_z^2$
E_-	$\binom{k_x}{k_y}$	$\binom{[k_x^2 - k_y^2]k_z}{k_x k_y k_z}$	$\binom{[k_x^2 - k_y^2]k_z^3}{k_x k_y k_z^3}$
	\times	$\binom{k_x k_z^2}{k_y k_z^2}$	$\binom{k_x k_z^4}{k_y k_z^4}$
	\times	\times	$\binom{k_x^5 - 10k_x^3 k_y^2 + 5k_x k_y^4}{5k_x^4 k_y - 10k_x^2 k_y^3 + k_y^5}$
	\times	\times	$\binom{[k_x^2 - k_y^2]^2 k_z - 4k_x^2 k_y^2 k_z}{k_x k_y k_z [k_x^2 - k_y^2]}$

SOC Hamiltonian must be Hermitian, the Hermiticity is ensured by applying proper symmetrization procedures. After a straightforward but lengthy algebraic process, the resulting TAM tensor matrices are summarized in Table XI.

The relevant TAM basis functions are obtained by substituting momentum components with TAM operators, i.e., $k_i \rightarrow \hat{J}_i$ for $i \in \{x, y, z\}$. To guarantee Hermitian structure, one must symmetrize products of these operators appropriately. For example, both k_z and the third-order polynomial $k_x^3 - 3k_x k_y^2$ transform as the $A_{1,-}$ irrep, as indicated in Table X. Interestingly, the corresponding TAM tensor matrices transform as $A_{2,-}$ representations, which contrasts with the momentum basis behavior, see

Table XI. This is given by

$$A_{1-} \rightarrow A_{2-} : \begin{cases} k_z \rightarrow \hat{J}_z, \\ k_x^3 - 3k_x k_y^2 \rightarrow [\hat{J}_x^3 - 3\hat{J}_x \hat{J}_y^2], \end{cases} \quad (C1)$$

$$E_+ \rightarrow E_+ : \begin{cases} (k_x k_z, k_y k_z) \rightarrow (\lceil \hat{J}_x \hat{J}_z \rceil, \lceil \hat{J}_y \hat{J}_z \rceil), \\ (k_x^2 - k_y^2, k_x k_y) \rightarrow (\hat{J}_x^2 - \hat{J}_y^2, \lceil \hat{J}_x \hat{J}_y \rceil). \end{cases} \quad (C2)$$

The multipolar SOC model Hamiltonian is given by

$$H_N = \sum_{\mathbf{k}} \hat{\psi}_{\mathbf{k}}^\dagger \hat{H}(\mathbf{k}) \hat{\psi}_{\mathbf{k}}, \quad (C3)$$

where $\hat{\psi}_{\mathbf{k}}$ is a 6×1 (4×1) spinor defined in the $j = 5/2$ ($3/2$) TAM basis given by

$$\hat{\psi}_{\mathbf{k}} = (c_{\mathbf{k}, 5/2}, c_{\mathbf{k}, 3/2}, c_{\mathbf{k}, 1/2}, c_{\mathbf{k}, -1/2}, c_{\mathbf{k}, -3/2}, c_{\mathbf{k}, -5/2})^T, \quad (C4)$$

$$\hat{\psi}_{\mathbf{k}} = (c_{\mathbf{k}, 3/2}, c_{\mathbf{k}, 1/2}, c_{\mathbf{k}, -1/2}, c_{\mathbf{k}, -3/2})^T, \quad (C5)$$

where $c_{\mathbf{k}, m_j}^\dagger$ ($c_{\mathbf{k}, m_j}$) denotes the fermionic creation (annihilation) operator associated with momentum \mathbf{k} and magnetic quantum number $m_j \in [-j, j]$. The Hamiltonian $\hat{H}(\mathbf{k})$ is a Hermitian matrix-valued function and any term appearing in it must result from a combination of momentum-dependent polynomials and TAM basis matrices that transform according to the trivial irrep $A_{1,+}$, satisfied by

$$\hat{g} \hat{H}(\hat{R}^{-1} \mathbf{k}) \hat{g}^\dagger \mapsto +\hat{H}(\mathbf{k}), \quad (C6)$$

where R^{-1} is the 3×3 orthogonal rotation matrix in momentum space and \hat{g} denotes the matrix form for symmetry elements of \mathcal{M}_{3v} .

Using Table IX, the multipolar SOC energy takes the form

$$\hat{H}(\mathbf{k}) = A_{1,+}^m \otimes A_{1,+}^j + A_{2,+}^m \otimes A_{2,+}^j + E_+^m \otimes E_+^j + A_{1,-}^m \otimes A_{1,-}^j + A_{2,-}^m \otimes A_{2,-}^j + E_-^m \otimes E_-^j, \quad (C7)$$

where $A_{1,+}^{m(j)}$ denotes the symmetry-allowed momentum-dependent polynomial (TAM tensor matrix) transforming according to the $A_{1,+}$ irrep, with the superscripts m and j labeling momentum and TAM contributions, respectively. The first line in $\hat{H}(\mathbf{k})$ is even under parity exchange while the second line are odd in momentum. These terms break inversion symmetry. After performing the necessary symmetry analysis and algebraic construction, we arrive at the explicit form of the even-parity SOC energy in the $j > 1/2$ basis, given by

$$A_{1,+}^m \otimes A_{1,+}^j = \sum_{i=1}^4 \mathbf{P}_i \cdot \mathbf{A}_{1+} [\hat{A}_{1+}]_i, \quad (C8)$$

$$A_{2,+}^m \otimes A_{2,+}^j = k_z (3k_y k_x^2 - k_y^3) [\lceil 3J_y J_x^2 - J_y^3 \rceil J_z], \quad (C9)$$

Table XI. Total angular momentum tensor matrices for $j > 1/2$ electrons transforming according to \mathcal{M}_{3v} point group.

$A_{1,+}$	\hat{J}_0	\hat{J}_z^2	$\lceil \llbracket \hat{J}_x^3 - 3\hat{J}_x\hat{J}_y^2 \rrbracket \hat{J}_z \rceil$
\times	\times		\hat{J}_z^4
$A_{2,+}$	\times	\times	$\lceil \llbracket 3\hat{J}_y\hat{J}_x^2 - \hat{J}_y^3 \rrbracket \hat{J}_z \rceil$
E_+	\times	$(\hat{J}_x^2 - \hat{J}_y^2)$	$(\lceil (\hat{J}_x^2 - \hat{J}_y^2)\hat{J}_z^2 \rceil)$
	\times	$(\lceil \hat{J}_x\hat{J}_y \rceil)$	$(\lceil \hat{J}_x\hat{J}_z^3 \rceil)$
$A_{1,-}$	\times	$\llbracket 3\hat{J}_y\hat{J}_x^2 - \hat{J}_y^3 \rrbracket$	$\lceil \llbracket 3\hat{J}_y\hat{J}_x^2 - \hat{J}_y^3 \rrbracket \hat{J}_z^2 \rceil$
$A_{2,-}$	\hat{J}_z	$\llbracket \hat{J}_x^3 - 3\hat{J}_x\hat{J}_y^2 \rrbracket$	$\lceil \llbracket \hat{J}_x^3 - 3\hat{J}_x\hat{J}_y^2 \rrbracket \hat{J}_z^2 \rceil$
	\times	\hat{J}_z^3	\hat{J}_z^5
E_-	(\hat{J}_x)	$(\lceil (\hat{J}_x^2 - \hat{J}_y^2)\hat{J}_z \rceil)$	$(\lceil (J_x^2 - J_y^2)J_z^3 \rceil)$
	\times	$(\lceil J_x J_z^2 \rceil)$	$(\lceil J_y J_z^4 \rceil)$

$$E_+^m \otimes E_+^j = \sum_{i=1}^4 \mathbf{N}_i \cdot (\mathbf{E}_+[\hat{\mathbf{E}}_+]_i + \mathbf{E}'_+[\hat{\mathbf{E}}'_+]_i). \quad (\text{C10})$$

Also, we have defined odd-parity terms in the normal state parts, which are given by

$$A_{1,-}^m \otimes A_{1,-}^j = \sum_{i=1}^2 \mathbf{T}_i \cdot \mathbf{A}_{1,-}[\hat{A}_{1,-}]_i, \quad (\text{C11})$$

$$A_{2,-}^m \otimes A_{2,-}^j = \sum_{i=1}^5 \mathbf{R}_i \cdot \mathbf{A}_{2,-}[\hat{A}_{2,-}]_i, \quad (\text{C12})$$

$$E_-^m \otimes E_-^j = \sum_{i=1}^5 \mathbf{G}_i \cdot (\mathbf{E}_-[\hat{\mathbf{E}}_-]_i + \mathbf{E}'_-[\hat{\mathbf{E}}'_-]_i), \quad (\text{C13})$$

Note that the full multipolar SOC Hamiltonian is a summation of odd- and even-parity terms. The TAM basis elements that are even under time-reversal symmetry are given by

$$\hat{A}_{1+} \equiv (\hat{J}_0, \hat{J}_z^2, \hat{J}_z^4 \lceil \llbracket \hat{J}_x^3 - 3\hat{J}_x\hat{J}_y^2 \rrbracket \hat{J}_z \rceil), \quad (\text{C14})$$

$$\hat{\mathbf{E}}_+ \equiv (\hat{J}_x^2 - \hat{J}_y^2, \lceil \hat{J}_x\hat{J}_z \rceil, \lceil (\hat{J}_x^2 - \hat{J}_y^2)\hat{J}_z^2 \rceil, \lceil \hat{J}_x\hat{J}_z^3 \rceil), \quad (\text{C15})$$

$$\hat{\mathbf{E}}'_+ \equiv (2\lceil \hat{J}_x\hat{J}_y \rceil, -\lceil \hat{J}_y\hat{J}_z \rceil, 2\lceil \lceil \hat{J}_x\hat{J}_y \rceil \hat{J}_z^2 \rceil, -\lceil \hat{J}_y\hat{J}_z^3 \rceil), \quad (\text{C16})$$

while the odd bases takes the form

$$\hat{A}_{1-} \equiv (\llbracket 3\hat{J}_y\hat{J}_x^2 - \hat{J}_y^3 \rrbracket, \lceil \llbracket 3\hat{J}_y\hat{J}_x^2 - \hat{J}_y^3 \rrbracket \hat{J}_z^2 \rceil), \quad (\text{C17})$$

$$\hat{A}_{2-} \equiv (\hat{J}_z, \llbracket \hat{J}_x^3 - 3\hat{J}_x\hat{J}_y^2 \rrbracket, \hat{J}_z^3, \lceil \llbracket \hat{J}_x^3 - 3\hat{J}_x\hat{J}_y^2 \rrbracket \hat{J}_z^2 \rceil, \hat{J}_z^5), \quad (\text{C18})$$

$$\hat{\mathbf{E}}_- \equiv (\hat{J}_y, \llbracket \hat{J}_x\hat{J}_y\hat{J}_z \rrbracket, \lceil \hat{J}_y\hat{J}_z^2 \rceil, \lceil \lceil \hat{J}_x\hat{J}_y \rceil \hat{J}_z^3 \rceil, \lceil \hat{J}_y\hat{J}_z^4 \rceil), \quad (\text{C19})$$

$$\hat{\mathbf{E}}'_- \equiv (\hat{J}_x, -\frac{\lceil \hat{J}_1\hat{J}_z \rceil}{2}, \lceil \hat{J}_x\hat{J}_z^2 \rceil, -\frac{\lceil \hat{J}_1\hat{J}_z^3 \rceil}{2}, \lceil \hat{J}_x\hat{J}_z^4 \rceil), \quad (\text{C20})$$

where $\hat{J}_1 \equiv \hat{J}_x^2 - \hat{J}_y^2$. Note that the coefficients of basis matrices in Eq. (C20) are obtained to let Eq. (C7)

transform according to A_{1+} irrep. In addition, the relevant momentum-dependent polynomials are also compactly written in multi-element vectors defined by

$$\mathbf{A}_{1+} \equiv (1, k_x^2 + k_y^2, k_z^2, k_z^4, k_z(k_x^3 - 3k_xk_y^2)), \quad (\text{C21})$$

$$\mathbf{E}_+ \equiv (k_xk_z, K_1, K_1k_z^2, [K_1^2 - 4K_2^2], k_xk_z^3), \quad (\text{C22})$$

$$\mathbf{E}'_+ \equiv (-k_yk_z, 2K_2, 2K_2k_z^2, -4K_1K_2, -k_yk_z^3), \quad (\text{C23})$$

where $K_1 \equiv k_x^2 - k_y^2$ and $K_2 \equiv k_xk_y$, and the odd parity form factors become

$$\mathbf{A}_{1-} \equiv (k_z, k_x^3 - 3k_xk_y^2, k_z^3, k_z^2(k_x^3 - 3k_xk_y^2), k_z^5), \quad (\text{C24})$$

$$\mathbf{A}_{2-} \equiv (k_y(3k_x^2 - k_y^2), k_y(3k_x^2 - k_y^2)k_z^2), \quad (\text{C25})$$

$$\mathbf{E}_- \equiv (k_x, K_1k_z, k_xk_z^2, (k_x^5 - 10k_x^3k_y^2 + 5k_xk_y^4), (K_1^2 - 4K_2^2)k_z, K_1k_z^3, k_xk_z^4), \quad (\text{C26})$$

$$\mathbf{E}'_- \equiv (-k_y, 2K_3, -k_yk_z^2, (k_y^5 - 10k_x^2k_y^3 + 5k_x^4k_y), -4K_1K_3, 2K_3k_z^2, -k_yk_z^4), \quad (\text{C27})$$

where $K_3 \equiv k_xk_yk_z$. Note that the coefficients of momentum basis in \mathbf{E}'_{\pm} are imposed by A_{1+} constraint. Moreover, in Eqs. (C8)–(C27), we have defined a multi-element vector of arbitrary coefficients to control the strength of momentum dependent polynomials in Eqs. (C21)–(C27) as

$$\mathbf{P}_i = (P_1^{(i)}, P_2^{(i)}, P_3^{(i)}, P_4^{(i)}, P_5^{(i)}), \quad (\text{C28})$$

$$\mathbf{N}_i = (n_1^{(i)}, n_2^{(i)}, n_3^{(i)}, n_4^{(i)}, n_5^{(i)}), \quad (\text{C29})$$

$$\mathbf{T}_i = (T_1^{(i)}, T_2^{(i)}, T_3^{(i)}, T_4^{(i)}, T_5^{(i)}), \quad (\text{C30})$$

$$\mathbf{R}_i = (R_1^{(i)}, R_2^{(i)}), \quad (\text{C31})$$

$$\mathbf{G}_i = (G_1^{(i)}, G_2^{(i)}, G_3^{(i)}, G_4^{(i)}, G_5^{(i)}, G_6^{(i)}, G_7^{(i)}). \quad (\text{C32})$$

Importantly, the above coefficients can be derived through matching the $\mathbf{k} \cdot \mathbf{p}$ model to the results of density functional theory.

Appendix D: Explicit form of effective Hamiltonians

In this part, we summarize the effective model Hamiltonians in $j \in \{1/2, 3/2, 5/2\}$ basis. In $j = 1/2$ basis, the full Hamiltonian includes four TAM basis matrices yielding

$$\hat{H}_{j=1/2}(\mathbf{k}) = C_{0,\mathbf{k}}\hat{J}_0 + C_{x,\mathbf{k}}\hat{J}_x + C_{y,\mathbf{k}}\hat{J}_y + C_{z,\mathbf{k}}\hat{J}_z, \quad (\text{D1})$$

where the momentum dependent polynomials are

$$C_{0,\mathbf{k}} = n_0 + n_1(k_x^2 + k_y^2) + n_2k_z^2, \quad (\text{D2})$$

$$C_{x,\mathbf{k}} = -\gamma_1k_y + \gamma_22k_xk_yk_z - \gamma_3k_yk_z^2 + \gamma_4(k_y^5 - 10k_x^2k_y^3 + 5k_x^4k_y), \quad (\text{D3})$$

$$C_{y,\mathbf{k}} = +\gamma_1k_x + \gamma_2(k_x^2 - k_y^2)k_z + \gamma_3k_xk_z^2 + \gamma_4(k_x^5 - 10k_x^2k_y^3 + 5k_x^4k_y), \quad (\text{D4})$$

$$C_{z,\mathbf{k}} = m_1(3k_y k_x^2 - k_y^3) + m_2((3k_y k_x^2 - k_y^3)k_z^2). \quad (\text{D5})$$

Here n_0 denotes the Fermi energy, n_1 (n_2) is the strength of the in-plane (out-of-plane) kinetic term, $C_{x(y),\mathbf{k}}$ encodes the components of Rashba SOC up to fifth-order momenta, where $\gamma_{1,2,3,4}$ control the strength of each term, and $C_{z,\mathbf{k}}$ denotes the SOC contribution with out-of-plane spin texture components.

Moreover, the effective Hamiltonian admits a much richer operator structure for higher total angular momentum. In a $(2j+1)$ -dimensional Hilbert space, the number of linearly independent Hermitian matrices is $(2j+1)^2$. Hence, there are 16 independent operator channels for $j = 3/2$ and 36 for $j = 5/2$. Accordingly, we expand the Hamiltonian as

$$\begin{aligned} \hat{H}(\mathbf{k}) = & \mathcal{A}_{1,\mathbf{k}} \hat{J}_0 + \mathcal{A}_{2,\mathbf{k}} \hat{J}_z^2 \\ & + \Lambda_{1,\mathbf{k}} \hat{J}_y + \Upsilon_{1,\mathbf{k}} \hat{J}_x \\ & + \Lambda_{2,\mathbf{k}} \lceil \hat{J}_y \hat{J}_z^2 \rceil + \Upsilon_{2,\mathbf{k}} \lceil \hat{J}_x \hat{J}_z^2 \rceil \\ & + \Lambda_{3,\mathbf{k}} \lceil \hat{J}_x \hat{J}_y \hat{J}_z \rceil + \frac{1}{2} \Upsilon_{3,\mathbf{k}} \lceil \lceil (\hat{J}_y^2 - \hat{J}_x^2) \hat{J}_z \rceil \rceil \\ & + \mathcal{B}_{1,\mathbf{k}} \hat{J}_z + \zeta_1 k_z (3 \lceil \hat{J}_y \hat{J}_x^2 \rceil - \hat{J}_y^3) \\ & + \mathcal{B}_{2,\mathbf{k}} \hat{J}_z^3 + \mathcal{B}_{3,\mathbf{k}} (\hat{J}_x^3 - 3 \lceil \hat{J}_x \hat{J}_y^2 \rceil) \\ & + \zeta_2 k_z \lceil (3 \lceil \hat{J}_y \hat{J}_x^2 \rceil - \hat{J}_y^3) \hat{J}_z^2 \rceil + \dots, \end{aligned} \quad (\text{D6})$$

where

$$\mathcal{B}_{i,\mathbf{k}} = m_{1,i} k_y (3k_x^2 - k_y^2) + m_{2,i} k_y (3k_x^2 - k_y^2) k_z^2, \quad (\text{D7})$$

and $\mathcal{A}_{i,\mathbf{k}}$, $\Lambda_{i,\mathbf{k}}$ and $\Upsilon_{i,\mathbf{k}}$ are defined in Eqs. (5), (15), and (16), respectively. All remaining symmetry-allowed contributions are obtained systematically by combining momentum-basis polynomials with TAM-tensor operators such that the resulting terms transform according to the $A_{1,+}$ irrep.

Appendix E: First-principle calculations

In this section, we briefly explain how to obtain the TAM texture from first-principle calculations. In practice, the Bloch spinors $|u_{n\mathbf{k}}\rangle$ can be obtained from a noncollinear SOC calculation in VASP [107, 108]. For noncollinear SOC case, the three components of the projected spin magnetization (Pauli-matrix expectation values) directly yield the usual $j = 1/2$ spin texture [109]. To obtain TAM textures in a target j -manifold (e.g. $j = 3/2$ for p -orbital), one should reconstruct the local spinor coefficients in the orbital-spin product basis $w_{im}^{n\mathbf{k}} = \langle i, lm_l \otimes m_s | u_{n\mathbf{k}} \rangle$, and rotate to the local $|jm_j\rangle$ basis using Clebsch–Gordan coefficients (CGCs). Finally, we can evaluate the projected expectation value \mathbf{J} .

The numerical simulation results in discrete \mathbf{k} -points, energy bands and how many ions are taken into account. The Wannier basis includes orbital and spin-1/2 degrees of freedom. Thus, we need to obtain the projection of

Wannier basis onto the TAM basis. The TAM operator is $\hat{\mathbf{J}} = \hat{\mathbf{L}} + \hat{\mathbf{S}}$, and for any normalized state $\langle \hat{\mathbf{J}} \rangle_{n\mathbf{k}} = \langle u_{n\mathbf{k}} | \hat{\mathbf{L}} | u_{n\mathbf{k}} \rangle + \langle u_{n\mathbf{k}} | \hat{\mathbf{S}} | u_{n\mathbf{k}} \rangle$ where $|u_{n\mathbf{k}}\rangle$ is the Bloch spinor wave function. A $j > 1/2$ manifold requires a projected TAM texture $\langle \hat{\mathbf{J}} \rangle_{n\mathbf{k}}^{(j)} = \langle u_{n\mathbf{k}} | P_j \hat{\mathbf{J}} P_j | u_{n\mathbf{k}} \rangle / \langle u_{n\mathbf{k}} | P_j | u_{n\mathbf{k}} \rangle$. The component of conventional spin-1/2 texture can be obtained by $\langle \hat{S}_i \rangle_{n\mathbf{k}} = (1/2) \sum_{\sigma\sigma'} (\hat{\sigma}_i)_{\sigma\sigma'} \langle u_{n\mathbf{k}}^\sigma | \hat{P} | u_{n\mathbf{k}}^{\sigma'} \rangle$ where $|u_{n\mathbf{k}}^\sigma\rangle$ is the weight for spinor component with spin degree of freedom $\sigma \in \{\uparrow, \downarrow\}$, $\hat{\sigma}_i$ is the i th Pauli matrix where $i \in \{x, y, z\}$, and \hat{P} denotes the local/orbital projector. For a heavy-element p or d manifold, the expansion of Bloch spinor in a localized basis takes the form $|lm_l \otimes \sigma\rangle \equiv |lm_l\rangle \otimes |\sigma\rangle$ in density functional theory (DFT). In this case, the periodic part of the Bloch state is

$$|u_{n\mathbf{k}}\rangle = \sum_{m_l, \sigma} c_{lm_l}^{sm_s} |lm_l \otimes sm_s\rangle, \quad (\text{E1})$$

where $c_{lm_l}^{sm_s} = \langle lm_l \otimes sm_s | u_{n\mathbf{k}} \rangle$ denotes the local orbital-spin weight for the projected Bloch state. The projection of spin-1/2 texture vector can be obtained by summation of its projection onto the real space basis as $\langle \mathbf{S} \rangle_{n\mathbf{k}} = (\hbar/2) \sum_i \langle u_{n\mathbf{k}} | \hat{P}_i \hat{\sigma} \hat{P}_i | u_{n\mathbf{k}} \rangle$ where \hat{P}_i is the matrix of projection onto the i th site.

Analogously, the TAM texture vector can be obtained likewise. For p -orbital ($l = 1$) with strong SOC, the relevant high- j manifold is the quartet $j = 3/2$ TAM. In this case, the relevant TAM texture is the average value of $\hat{\mathbf{J}} = (\hat{J}_x, \hat{J}_y, \hat{J}_z)$ projected to the $j = 3/2$ subspace at site i as defined by $\langle \hat{\mathbf{J}} \rangle_{ijn\mathbf{k}}$. This projection is $\hat{P}_{ij} = \sum_{m_j} |ijm_j\rangle \langle ijm_j|$ where \hat{P}_{ij} is Hermitian $\hat{P}_{ij}^\dagger = \hat{P}_{ij}$ and fulfills $\hat{P}_{ij}^2 = \hat{P}_{ij}$. This projector keeps only the j degrees of freedom on the site index i . Under this projection the normalized Bloch state takes the form $|\psi_{ij}^{n\mathbf{k}}\rangle = (\hat{P}_{ij} / \langle \hat{P}_{ij} \rangle_{n\mathbf{k}})^{1/2} |u_{n\mathbf{k}}\rangle$ where the site-resolved TAM texture becomes

$$\langle \hat{\mathbf{J}} \rangle_{n\mathbf{k}}^{ij} \equiv \frac{1}{\langle \hat{P}_{ij} \rangle_{n\mathbf{k}}} \langle u_{n\mathbf{k}} | \hat{P}_{ij} \hat{\mathbf{J}} \hat{P}_{ij} | u_{n\mathbf{k}} \rangle. \quad (\text{E2})$$

In the DFT/Wannier basis the local- j state can be obtained through the expansion $|ijm_j\rangle = \sum_{m_l m_s} C_{lm_l m_s}^{j m_j} |ilm_l \otimes m_s\rangle$ where $C_{lm_l m_s}^{j m_j} = \langle lm_l m_s | jm_j \rangle$ is the CGC and $|ilm_l \otimes m_s\rangle$ is the Wannier state labeled with site i , orbital l (m_l quantum number), and spin $m_s \in \{\uparrow, \downarrow\}$ degrees of freedom. Under this linear expansion, the local j -space projector is equivalent to

$$\hat{P}_{ij} = \sum_{mm'} \mathcal{C}_m^{m'} |im\rangle \langle im'|, \quad (\text{E3})$$

where $m = (m_l, m_s)$ and $|im\rangle \equiv |ilm_l \otimes m_s\rangle$, $\mathcal{C}_{mm'}^{m_j} \equiv C_m^{m_j} (C_{m'}^{m_j})^*$ is the product of CGCs, and $\mathcal{C}_m^{m'} = \sum_{m_j} \mathcal{C}_{mm'}^{m_j}$. In the case, the site-resolved average of TAM becomes

$$\langle \hat{\mathbf{J}} \rangle_{n\mathbf{k}}^{ij} = \frac{1}{N} \sum_{m_1 m_2 m_3 m_4} \sum_{m_2 m_3 m_4} \mathcal{C}_{m_1}^{m_2} \mathcal{C}_{m_3}^{m_4} (w_{im_1}^{n\mathbf{k}})^* w_{im_4}^{n\mathbf{k}} (J_{i\alpha})_{m_2 m_3}, \quad (\text{E4})$$

where \mathcal{N} is the normalization factor, $w_{im}^{n\mathbf{k}} = \langle im|u_{n\mathbf{k}}\rangle$, and the matrix element for the TAM matrices is

$$(J_{i\alpha})_{mm'} = (L_{i\alpha})_{m_l m'_l} \delta_{m_s m'_s} + \delta_{m_l m'_l} (s_{i\alpha})_{m_s m'_s}, \quad (\text{E5})$$

where $(O_{i\alpha})_{mm'}$ with $O \in \{L, s\}$ denotes the matrix element of local orbital and spin.

[1] T. Ando, A. B. Fowler, and F. Stern, Electronic properties of two-dimensional systems, *Rev. Mod. Phys.* **54**, 437 (1982).

[2] I. Žutić, J. Fabian, and S. Das Sarma, Spintronics: Fundamentals and applications, *Rev. Mod. Phys.* **76**, 323 (2004).

[3] S. E. Barnes, J. Ieda, and S. Maekawa, Rashba spin-orbit anisotropy and the electric field control of magnetism, *Sci. Rep.* **4**, 4105 (2014).

[4] B. Dieny and M. Chshiev, Perpendicular magnetic anisotropy at transition metal/oxide interfaces and applications, *Rev. Mod. Phys.* **89**, 025008 (2017).

[5] J. A. Sobota, Y. He, and Z.-X. Shen, Angle-resolved photoemission studies of quantum materials, *Rev. Mod. Phys.* **93**, 025006 (2021).

[6] G. F. Quinteiro Rosen, P. I. Tamborenea, and T. Kuhn, Interplay between optical vortices and condensed matter, *Rev. Mod. Phys.* **94**, 035003 (2022).

[7] G. Burkard, T. D. Ladd, A. Pan, J. M. Nichol, and J. R. Petta, Semiconductor spin qubits, *Rev. Mod. Phys.* **95**, 025003 (2023).

[8] M. Amundsen, J. Linder, J. W. A. Robinson, I. Žutić, and N. Banerjee, Colloquium: Spin-orbit effects in superconducting hybrid structures, *Rev. Mod. Phys.* **96**, 021003 (2024).

[9] X.-L. Qi, T. L. Hughes, and S.-C. Zhang, Topological field theory of time-reversal invariant insulators, *Phys. Rev. B* **78**, 195424 (2008).

[10] M. Wu, J. Jiang, and M. Weng, Spin dynamics in semiconductors, *Phys. Rep.* **493**, 61 (2010).

[11] M. Z. Hasan and C. L. Kane, Colloquium: Topological insulators, *Rev. Mod. Phys.* **82**, 3045 (2010).

[12] C. Fang, M. J. Gilbert, X. Dai, and B. A. Bernevig, Multi-Weyl topological semimetals stabilized by point group symmetry, *Phys. Rev. Lett.* **108**, 266802 (2012).

[13] H. Weng, C. Fang, Z. Fang, B. A. Bernevig, and X. Dai, Weyl semimetal phase in noncentrosymmetric transition-metal monophosphides, *Phys. Rev. X* **5**, 011029 (2015).

[14] S.-Y. Xu, I. Belopolski, D. S. Sanchez, C. Zhang, G. Chang, C. Guo, G. Bian, Z. Yuan, H. Lu, T.-R. Chang, P. P. Shibayev, M. L. Prokopovych, N. Alidoust, H. Zheng, C.-C. Lee, S.-M. Huang, R. Sankar, F. Chou, C.-H. Hsu, H.-T. Jeng, A. Bansil, T. Neupert, V. N. Strocov, H. Lin, S. Jia, and M. Z. Hasan, Experimental discovery of a topological Weyl semimetal state in TaP, *Sci. Adv.* **1**, e1501092 (2015).

[15] T. M. McCormick, I. Kimchi, and N. Trivedi, Minimal models for topological Weyl semimetals, *Phys. Rev. B* **95**, 075133 (2017).

[16] S. Borisenko, D. Evtushinsky, Q. Gibson, A. Yaresko, K. Koepernik, T. Kim, M. Ali, J. van den Brink, M. Hoesch, A. Fedorov, E. Haubold, Y. Kushnirenko, I. Soldatov, R. Schäfer, and R. J. Cava, Time-reversal symmetry breaking type-II Weyl state in YbMnBi₂, *Nature Commun.* **10**, 3424 (2019).

[17] D. Go, J.-P. Hanke, P. M. Buhl, F. Freimuth, G. Bihlmayer, H.-W. Lee, Y. Mokrousov, and S. Blügel, Toward surface orbitronics: giant orbital magnetism from the orbital Rashba effect at the surface of sp-metals, *Sci. Rep.* **7**, 46742 (2017).

[18] D. Ralph and M. Stiles, Spin transfer torques, *J. Magn. Magn. Mat.* **320**, 1190 (2008).

[19] A. Manchon, J. Železný, I. M. Miron, T. Jungwirth, J. Sinova, A. Thiaville, K. Garello, and P. Gambardella, Current-induced spin-orbit torques in ferromagnetic and antiferromagnetic systems, *Rev. Mod. Phys.* **91**, 035004 (2019).

[20] E. Saitoh, M. Ueda, H. Miyajima, and G. Tatara, Conversion of spin current into charge current at room temperature: Inverse spin-Hall effect, *Apl. Phys. Lett.* **88**, 182509 (2006).

[21] T. Yoda, T. Yokoyama, and S. Murakami, Current-induced orbital and spin magnetizations in crystals with helical structure, *Sci. Rep.* **5**, 12024 (2015).

[22] L. Fu, Hexagonal warping effects in the surface states of the topological insulator Bi₂Te₃, *Phys. Rev. Lett.* **103**, 266801 (2009).

[23] S. Vajna, E. Simon, A. Szilva, K. Palotas, B. Ujfaluassy, and L. Szunyogh, Higher-order contributions to the Rashba-Bychkov effect with application to the Bi/Ag(111) surface alloy, *Phys. Rev. B* **85**, 075404 (2012).

[24] R. Moriya, K. Sawano, Y. Hoshi, S. Masubuchi, Y. Shiraki, A. Wild, C. Neumann, G. Abstreiter, D. Bougeard, Y. Koga, and T. Machida, Cubic Rashba spin-orbit interaction of a two-dimensional hole gas in a strained-Ge/SiGe quantum well, *Phys. Rev. Lett.* **113**, 086601 (2014).

[25] K. Miyamoto, H. Miyahara, K. Kuroda, T. Maegawa, A. Kimura, and T. Okuda, Peculiar Rashba spin texture induced by *C*_{3v} symmetry on the Bi(111) surface revisited, *Phys. Rev. B* **97**, 085433 (2018).

[26] M.-C. Hsu, L.-Z. Yao, S. G. Tan, C.-R. Chang, G. Liang, and M. B. A. Jalil, Inherent orbital spin textures in Rashba effect and their implications in spin-orbitronics, *J. Phys.: Condens. Matter* **30**, 285502 (2018).

[27] H. C. Koo, S. B. Kim, H. Kim, T.-E. Park, J. W. Choi, K.-W. Kim, G. Go, J. H. Oh, D.-K. Lee, E.-S. Park, I.-S. Hong, and K.-J. Lee, Rashba effect in functional spintronic devices, *Adv. Mat.* **32**, 2002117 (2020).

[28] S. Sheoran, M. Kumar, P. Bhumla, and S. Bhattacharya, Rashba spin splitting and anomalous spin textures in the bulk ferroelectric oxide perovskite KIO₃, *Mater. Adv.* **3**, 4170 (2022).

[29] T. Frank, P. E. Faria Junior, K. Zollner, and J. Fabian, Emergence of radial Rashba spin-orbit fields in twisted van der Waals heterostructures, *Phys. Rev. B* **109**, L241403 (2024).

[30] A. Jain, G. Goyal, and D. K. Singh, Weyl semimetal-

lic state with antiferromagnetic order in the Rashba-Hubbard model, *Phys. Rev. B* **110**, 075134 (2024).

[31] S. Gujarathi, K. M. Alam, and S. Pramanik, Magnetic-field-induced spin texture in a quantum wire with linear Dresselhaus spin-orbit coupling, *Phys. Rev. B* **85**, 045413 (2012).

[32] F. Kirtschig, J. van den Brink, and C. Ortix, Surface-state spin textures in strained bulk HgTe: Strain-induced topological phase transitions, *Phys. Rev. B* **94**, 235437 (2016).

[33] L. L. Tao, T. R. Paudel, A. A. Kovalev, and E. Y. Tsymbal, Reversible spin texture in ferroelectric HfO₂, *Phys. Rev. B* **95**, 245141 (2017).

[34] H. J. Zhao, H. Nakamura, R. Arras, C. Paillard, P. Chen, J. Gosteau, X. Li, Y. Yang, and L. Bellaiche, Purely cubic spin splittings with persistent spin textures, *Phys. Rev. Lett.* **125**, 216405 (2020).

[35] H. J. Zhao, P. Chen, C. Paillard, R. Arras, Y.-W. Fang, X. Li, J. Gosteau, Y. Yang, and L. Bellaiche, Large spin splittings due to the orbital degree of freedom and spin textures in a ferroelectric nitride perovskite, *Phys. Rev. B* **102**, 041203 (2020).

[36] D. Y. Usachov, I. A. Nechaev, G. Poelchen, M. Gütter, E. E. Krasovskii, S. Schulz, A. Generalov, K. Kliemt, A. Kraiker, C. Krellner, K. Kummer, S. Danzenbächer, C. Laubschat, A. P. Weber, J. Sánchez-Barriga, E. V. Chulkov, A. F. Santander-Syro, T. Imai, K. Miyamoto, T. Okuda, and D. V. Vyalikh, Cubic Rashba effect in the surface spin structure of rare-earth ternary materials, *Phys. Rev. Lett.* **124**, 237202 (2020).

[37] G. Dresselhaus, Spin-orbit coupling effects in Zinc blende structures, *Phys. Rev.* **100**, 580 (1955).

[38] J. M. Luttinger, Quantum theory of cyclotron resonance in semiconductors: General theory, *Phys. Rev.* **102**, 1030 (1956).

[39] R. Winkler, *Spin-Orbit Coupling Effects in Two-Dimensional Electron and Hole Systems*, Springer Tracts in Modern Physics, Vol. 191 (Springer, Berlin, 2003).

[40] R. Winkler, Spin density matrix of spin- $\frac{3}{2}$ hole systems, *Phys. Rev. B* **70**, 125301 (2004).

[41] B. Bradlyn, J. Cano, Z. Wang, M. G. Vergniory, C. Felser, R. J. Cava, and B. A. Bernevig, Beyond dirac and Weyl fermions: Unconventional quasiparticles in conventional crystals, *Science* **353**, aaf5037 (2016).

[42] P. M. R. Brydon, L. Wang, M. Weinert, and D. F. Agterberg, Pairing of $j = 3/2$ fermions in half-Heusler superconductors, *Phys. Rev. Lett.* **116**, 177001 (2016).

[43] D. F. Agterberg, P. M. R. Brydon, and C. Timm, Bogoliubov Fermi surfaces in superconductors with broken time-reversal symmetry, *Phys. Rev. Lett.* **118**, 127001 (2017).

[44] H. Kim, K. Wang, Y. Nakajima, R. Hu, S. Ziemak, P. Syers, L. Wang, H. Hodovanets, J. D. Denlinger, P. M. R. Brydon, D. F. Agterberg, M. A. Tanatar, R. Prozorov, and J. Paglione, Beyond triplet: Unconventional superconductivity in a spin-3/2 topological semimetal, *Sci. Adv.* **4**, eaao4513 (2018).

[45] I. Boettcher and I. F. Herbut, Unconventional superconductivity in luttinger semimetals: Theory of complex tensor order and the emergence of the uniaxial nematic state, *Phys. Rev. Lett.* **120**, 057002 (2018).

[46] B. Roy, S. A. A. Ghorashi, M. S. Foster, and A. H. Nevidomskyy, Topological superconductivity of spin-3/2 carriers in a three-dimensional doped Luttinger semimetal, *Phys. Rev. B* **99**, 054505 (2019).

[47] H. Menke, C. Timm, and P. M. R. Brydon, Bogoliubov Fermi surfaces stabilized by spin-orbit coupling, *Phys. Rev. B* **100**, 224505 (2019).

[48] G. Sim, A. Mishra, M. J. Park, Y. B. Kim, G. Y. Cho, and S. Lee, Multipolar superconductivity in Luttinger semimetals, *Phys. Rev. Res.* **2**, 023416 (2020).

[49] C. Timm and A. Bhattacharya, Symmetry, nodal structure, and Bogoliubov Fermi surfaces for nonlocal pairing, *Phys. Rev. B* **104**, 094529 (2021).

[50] M. Bahari, S.-B. Zhang, C.-A. Li, S.-J. Choi, P. Rüßmann, C. Timm, and B. Trauzettel, Helical topological superconducting pairing at finite excitation energies, *Phys. Rev. Lett.* **132**, 266201 (2024).

[51] V. Edelstein, Spin polarization of conduction electrons induced by electric current in two-dimensional asymmetric electron systems, *Solid State Commun.* **73**, 233 (1990).

[52] R. H. Silsbee, Theory of the detection of current-induced spin polarization in a two-dimensional electron gas, *Phys. Rev. B* **63**, 155305 (2001).

[53] P. Gambardella and I. M. Miron, Current-induced spin-orbit torques, *Phil. Trans. Royal Society A* **369**, 3175 (2011).

[54] K. Shen, G. Vignale, and R. Raimondi, Microscopic theory of the inverse Edelstein effect, *Phys. Rev. Lett.* **112**, 096601 (2014).

[55] K. Ishizaka, M. S. Bahramy, H. Murakawa, M. Sakano, T. Shimojima, T. Sonobe, K. Koizumi, S. Shin, H. Miyahara, A. Kimura, K. Miyamoto, T. Okuda, H. Namatame, M. Taniguchi, R. Arita, N. Nagaosa, K. Kobayashi, Y. Murakami, R. Kumai, Y. Kaneko, Y. Onose, and Y. Tokura, Giant Rashba-type spin splitting in bulk BiTeI, *Nature Mat.* **10**, 521 (2011).

[56] Y. Feng, Q. Jiang, B. Feng, M. Yang, T. Xu, W. Liu, X. Yang, M. Arita, E. F. Schwier, K. Shimada, H. O. Jeschke, R. Thomale, Y. Shi, X. Wu, S. Xiao, S. Qiao, and S. He, Rashba-like spin splitting along three momentum directions in trigonal layered PtBi₂, *Nature Commun.* **10**, 4765 (2019).

[57] S. Li, Y. Luo, Q. Chen, W. Lv, Y. Song, L. Liu, X. Zhao, W. Liu, B. Zhang, and Z. Zeng, Large spin-orbit torque efficiency in PtBi₂ film, *Apl. Phys. Lett.* **119**, 132402 (2021).

[58] A. Veyrat, V. Labracherie, D. L. Bashlakov, F. Caglieris, J. I. Facio, G. Shipunov, T. Charvin, R. Acharya, Y. Naidyuk, R. Giraud, J. van den Brink, B. Büchner, C. Hess, S. Aswartham, and J. Dufouleur, Berezinskii-Kosterlitz-Thouless transition in the type-I Weyl semimetal PtBi₂, *Nano Lett.* **23**, 1229 (2023).

[59] A. Zhu, Z. Chen, M. Han, X. Liu, X. Chen, Y. Han, G. Zheng, X. Zhu, W. Gao, and M. Tian, Planar Hall effect in triply degenerate semimetal trigonal layered PtBi₂, *Phys. Rev. B* **110**, 125148 (2024).

[60] L. Bawden, J. M. Riley, C. H. Kim, R. Sankar, E. J. Monkman, D. E. Shai, H. I. Wei, E. B. Lochocki, J. W. Wells, W. Meevasana, T. K. Kim, M. Hoesch, Y. Ohtsubo, P. L. Fèvre, C. J. Fennie, K. M. Shen, F. Chou, and P. D. C. King, Hierarchical spin-orbital polarization of a giant Rashba system, *Sci. Adv.* **1**, e1500495 (2015).

[61] R. Vocaturo, K. Koepernik, J. I. Facio, C. Timm, I. C. Fulga, O. Janson, and J. van den Brink, Electronic structure of the surface-superconducting Weyl semimetal PtBi₂, *Phys. Rev. B* **110**, 054504 (2024).

[62] S. Palumbo, P. S. Cornaglia, and J. I. Facio, Interplay between inversion and translation symmetries in trigonal PtBi₂, *Phys. Rev. B* **112**, 205125 (2025).

[63] S. Changdar, O. Suvorov, A. Kuibarov, S. Thirupathaiah, G. Shipunov, S. Aswartham, S. Wurmehl, I. Kovalchuk, K. Koepernik, C. Timm, B. Büchner, I. C. Fulga, S. Borisenko, and J. van den Brink, Topological nodal i-wave superconductivity in PtBi₂, *Nature* **647**, 613 (2025).

[64] A. Kuibarov, O. Suvorov, R. Vocaturo, A. Fedorov, R. Lou, L. Merkowitz, V. Voroshnin, J. I. Facio, K. Koepernik, A. Yaresko, G. Shipunov, S. Aswartham, J. van den Brink, B. Büchner, and S. Borisenko, Evidence of superconducting Fermi arcs, *Nature* **626**, 294 (2024).

[65] X. Huang, L. Zhao, S. Schimmel, J. Besproswanny, P. Härtl, C. Hess, B. Büchner, and M. Bode, Sizable superconducting gap and anisotropic chiral topological superconductivity in the Weyl semimetal PtBi₂, *arXiv:2507.13843* (2025).

[66] K. Mæland, M. Bahari, and B. Trauzettel, Phonon-mediated intrinsic topological superconductivity in Fermi arcs, *Phys. Rev. B* **112**, 104507 (2025).

[67] H. Waje, F. Jakubczyk, J. van den Brink, and C. Timm, Ginzburg-Landau theory for unconventional surface superconductivity in PtBi₂, *Phys. Rev. B* **112**, 144519 (2025).

[68] K. Mæland, G. Sangiovanni, and B. Trauzettel, Mechanism for Nodal Topological Superconductivity on PtBi₂ Surface, *arXiv:2512.09994* (2025).

[69] A. Johansson, J. Henk, and I. Mertig, Edelstein effect in Weyl semimetals, *Phys. Rev. B* **97**, 085417 (2018).

[70] L. Salemi, M. Berritta, A. K. Nandy, and P. M. Oppeneer, Orbitally dominated Rashba-Edelstein effect in noncentrosymmetric antiferromagnets, *Nature Commun.* **10**, 5381 (2019).

[71] H. Isshiki, P. Muduli, J. Kim, K. Kondou, and Y. Otani, Phenomenological model for the direct and inverse Edelstein effects, *Phys. Rev. B* **102**, 184411 (2020).

[72] I. Gaiardoni, M. Trama, A. Maiellaro, C. Guarcello, F. Romeo, and R. Citro, Edelstein effect in isotropic and anisotropic Rashba models, *Condensed Matter* **10**, 10.3390/condmat10010015 (2025).

[73] W. Pan and J. Fabian, Tunable Edelstein effect in intrinsic two-dimensional ferroelectric metal PtBi₂, *arXiv:2601.16980* (2026).

[74] G. Koster, *Properties of the Thirty-two Point Groups*, M.I.T. Press research monographs (M.I.T. Press, 1963).

[75] H. T. Stokes and D. M. Hatch, *Isotropy Subgroups of the 230 Crystallographic Space Groups* (WORLD SCIENTIFIC, 1989).

[76] J. T. Hougen, Double group considerations, jahn-teller induced rovibronic effects, and the nuclear spin-electron spin hyperfine hamiltonian for a molecule of symmetry C_{3v} in an electronic ²E state, *J. Molec. Spectr.* **81**, 73 (1980).

[77] S. L. Altmann and P. Herzig, *Point-Group Theory Tables* (Clarendon Press, Oxford, 1994).

[78] W. Setyawan and S. Curtarolo, High-throughput electronic band structure calculations: Challenges and tools, *Comput. Mater. Sci.* **49**, 299 (2010).

[79] G. Katzer, Character tables, Gernot Katzer's SPICE Pages, available at http://gernot-katzers-spice-pages.com/character_tables/ (accessed 26 November 2025).

[80] H. Bentmann, S. Abdelouahed, M. Mulazzi, J. Henk, and F. Reinert, Direct observation of interband spin-orbit coupling in a two-dimensional electron system, *Phys. Rev. Lett.* **108**, 196801 (2012).

[81] R. Noguchi, K. Kuroda, K. Yaji, K. Kobayashi, M. Sakano, A. Harasawa, T. Kondo, F. Komori, and S. Shin, Direct mapping of spin and orbital entangled wave functions under interband spin-orbit coupling of giant Rashba spin-split surface states, *Phys. Rev. B* **95**, 041111 (2017).

[82] Z. Li, F. Marsiglio, and J. P. Carbotte, Vanishing of interband light absorption in a persistent spin helix state, *Sci. Rep.* **3**, 2828 (2013).

[83] K. Samokhin, On the effective models of spin-orbit coupling in a two-dimensional electron gas, *Ann. Phys.* **437**, 168710 (2022).

[84] Z. Alpichshev, J. G. Analytis, J.-H. Chu, I. R. Fisher, Y. L. Chen, Z. X. Shen, A. Fang, and A. Kapitulnik, Stm imaging of electronic waves on the surface of Bi₂Te₃: Topologically protected surface states and hexagonal warping effects, *Phys. Rev. Lett.* **104**, 016401 (2010).

[85] Y. H. Wang, D. Hsieh, D. Pilon, L. Fu, D. R. Gardner, Y. S. Lee, and N. Gedik, Observation of a warped helical spin texture in Bi₂Se₃ from circular dichroism angle-resolved photoemission spectroscopy, *Phys. Rev. Lett.* **107**, 207602 (2011).

[86] M. Koshino and E. McCann, Trigonal warping and Berry's phase $N\pi$ in abc-stacked multilayer graphene, *Phys. Rev. B* **80**, 165409 (2009).

[87] Y. Ikeda and Y. Yanase, Giant surface Edelstein effect in *d*-wave superconductors, *Phys. Rev. B* **102**, 214510 (2020).

[88] Y. Liu, J. Wang, Q. Sun, Y. Li, F. Liu, and F. Pan, Spintronics in two-dimensional materials, *Nano-Micro Lett.* **12**, 93 (2020).

[89] J. Q. Li and C. M. Wang, Edelstein effect in pseudospin Dirac systems, *Phys. Rev. B* **103**, 085401 (2021).

[90] K. Tenzin, A. Roy, H. Jafari, B. Banas, F. T. Cerasoli, M. Date, A. Jayaraj, M. Buongiorno Nardelli, and J. Ślawińska, Analogs of Rashba-Edelstein effect from density functional theory, *Phys. Rev. B* **107**, 165140 (2023).

[91] A. Roy, F. T. Cerasoli, A. Jayaraj, K. Tenzin, M. B. Nardelli, and J. Ślawińska, Long-range current-induced spin accumulation in chiral crystals, *npj Comput. Mat.* **8**, 243 (2022).

[92] S. LaShell, B. A. McDougall, and E. Jensen, Spin splitting of an Au(111) surface state band observed with angle resolved photoelectron spectroscopy, *Phys. Rev. Lett.* **77**, 3419 (1996).

[93] B. T. Thole, P. Carra, F. Sette, and G. van der Laan, X-ray circular dichroism as a probe of orbital magnetization, *Phys. Rev. Lett.* **68**, 1943 (1992).

[94] P. Carra, B. T. Thole, M. Altarelli, and X. Wang, X-ray circular dichroism and local magnetic fields, *Phys. Rev. Lett.* **70**, 694 (1993).

[95] A. Kotani and S. Shin, Resonant inelastic X-ray scattering spectra for electrons in solids, *Rev. Mod. Phys.* **73**, 203 (2001).

[96] L. J. P. Ament, M. van Veenendaal, T. P. Devreux, J. P. Hill, and J. van den Brink, Resonant inelastic X-ray scattering studies of elementary excitations, *Rev. Mod. Phys.* **83**, 705 (2011).

[97] S. Bhowal and N. A. Spaldin, Ferroically ordered magnetic octupoles in *d*-wave altermagnets, *Phys. Rev. X* **14**, 011019 (2024).

[98] U. Staub, C. Piamonteze, M. Garganourakis, S. P. Collins, S. M. Koohpayeh, D. Fort, and S. W. Lovesey, Ferromagnetic-type order of atomic multipoles in the polar ferrimagnetic GaFeO_3 , *Phys. Rev. B* **85**, 144421 (2012).

[99] J. Töpfer, B. Pawłowski, H. Beer, K. Plötner, P. Hofmann, and J. Herrfurth, Multi-pole magnetization of nd- feb magnets for magnetic micro-actuators and its characterization with a magnetic field mapping device, *J. Magn. Magn. Mat.* **270**, 124 (2004).

[100] H. Kontani, T. Tanaka, D. S. Hirashima, K. Yamada, and J. Inoue, Giant intrinsic spin and orbital Hall effects in Sr_2MO_4 ($M = \text{Ru, Rh, Mo}$), *Phys. Rev. Lett.* **100**, 096601 (2008).

[101] T. Tanaka, H. Kontani, M. Naito, T. Naito, D. S. Hirashima, K. Yamada, and J. Inoue, Intrinsic spin Hall effect and orbital Hall effect in 4*d* and 5*d* transition metals, *Phys. Rev. B* **77**, 165117 (2008).

[102] D. Go, D. Jo, H.-W. Lee, M. Klaeui, and Y. Mokrousov, Orbitronics: Orbital currents in solids, *Europhys. Lett.* **135**, 37001 (2021).

[103] G. Sala and P. Gambardella, Giant orbital Hall effect and orbital-to-spin conversion in 3*d*, 5*d*, and 4*f* metallic heterostructures, *Phys. Rev. Res.* **4**, 033037 (2022).

[104] Y.-G. Choi, D. Jo, K.-H. Ko, D. Go, K.-H. Kim, H. G. Park, C. Kim, B.-C. Min, G.-M. Choi, and H.-W. Lee, Observation of the orbital Hall effect in a light metal Ti, *Nature* **619**, 52 (2023).

[105] S. Ding, M.-G. Kang, W. Legrand, and P. Gambardella, Orbital torque in rare-earth transition-metal ferrimagnets, *Phys. Rev. Lett.* **132**, 236702 (2024).

[106] T. P. Cysne, L. M. Canonica, M. Costa, R. B. Muniz, and T. G. Rappoport, Orbitronics in two-dimensional materials, *npj Spintronics* **3**, 39 (2025).

[107] G. Kresse and J. Furthmüller, Efficient iterative schemes for ab initio total-energy calculations using a plane-wave basis set, *Phys. Rev. B* **54**, 11169 (1996).

[108] G. Kresse and D. Joubert, From ultrasoft pseudopotentials to the projector augmented-wave method, *Phys. Rev. B* **59**, 1758 (1999).

[109] For noncollinear SOC in the spin-1/2 basis, see **PROCAR** (VASP Wiki).